Mutations in the Kinesin-2 Motor *KIF3B* Cause an Autosomal-Dominant Ciliopathy

Benjamin Cogné,[1,2,19] Xenia Latypova,[1,2,3,19] Lokuliyanage Dona Samudita Senaratne,[4,19] Ludovic Martin,[5,19] Daniel C. Koboldt,[6] Georgios Kellaris,[3] Lorraine Fievet,[3] Guylène Le Meur,[7] Dominique Caldari,[8] Dominique Debray,[9] Mathilde Nizon,[1,2] Eirik Frengen,[4] Sara J. Bowne,[10] 99 Lives Consortium, Elizabeth L. Cadena,[10] Stephen P. Daiger,[10,11] Kinga M. Bujakowska,[12] Eric A. Pierce,[12] Michael Gorin,[13] Nicholas Katsanis,[3,14,15] Stéphane Bézieau,[1,2] Simon M. Petersen-Jones,[16] Laurence M. Occelli,[16] Leslie A. Lyons,[17] Laurence Legeai-Mallet,[5,18,20] Lori S. Sullivan,[10,20] Erica E. Davis,[3,14,15,20,*] and Bertrand Isidor[1,2,20,*]

Kinesin-2 enables ciliary assembly and maintenance as an anterograde intraflagellar transport (IFT) motor. Molecular motor activity is driven by a heterotrimeric complex comprised of KIF3A and KIF3B or KIF3C plus one non-motor subunit, KIFAP3. Using exome sequencing, we identified heterozygous *KIF3B* variants in two unrelated families with hallmark ciliopathy phenotypes. In the first family, the proband presents with hepatic fibrosis, retinitis pigmentosa, and postaxial polydactyly; he harbors a *de novo* c.748G>C (p.Glu250Gln) variant affecting the kinesin motor domain encoded by *KIF3B*. The second family is a six-generation pedigree affected predominantly by retinitis pigmentosa. Affected individuals carry a heterozygous c.1568T>C (p.Leu523Pro) *KIF3B* variant segregating in an autosomal-dominant pattern. We observed a significant increase in primary cilia length *in vitro* in the context of either of the two mutations while variant KIF3B proteins retained stability indistinguishable from wild type. Furthermore, we tested the effects of *KIF3B* mutant mRNA expression in the developing zebrafish retina. In the presence of either missense variant, rhodopsin was sequestered to the photoreceptor rod inner segment layer with a concomitant increase in photoreceptor cilia length. Notably, impaired rhodopsin trafficking is also characteristic of recessive *KIF3B* models as exemplified by an early-onset, autosomal-recessive, progressive retinal degeneration in Bengal cats; we identified a c.1000G>A (p.Ala334Thr) *KIF3B* variant by genome-wide association study and whole-genome sequencing. Together, our genetic, cell-based, and *in vivo* modeling data delineate an autosomal-dominant syndromic retinal ciliopathy in humans and suggest that multiple KIF3B pathomechanisms can impair kinesin-driven ciliary transport in the photoreceptor.

Kinesin family (KIF) genes encode a superfamily of microtubule-based molecular motors that transport intracellular cargo. Pathogenic variants in KIF-encoding loci have been associated with at least 14 distinct Mendelian disorders in humans, transmitted in both dominant or recessive inheritance fashions.[1] One unifying feature of autosomal-dominant KIF-related disorders is the primary impact on the central nervous system as evidenced by phenotypes such as intellectual disability (*KIF1A* [MIM: 614255]), cortical dysplasia (*KIF2A* [MIM: 615411]), spastic paraplegia (*KIF5A* [MIM: 604187]), and microcephaly (*KIF11* [MIM: 152950]). KIF genes mutated in autosomal-recessive disorders also impair neurological development and have been reported in X-linked intellectual disability (*KIF4A* [MIM: 300521]) or syndromic ciliopathies such as Acrocallosal syndrome (*KIF7* [MIM: 200990]) and Meckel syndrome (*KIF14* [MIM: 616258]).

Kinesin-2 subfamily motors, not currently associated with human disease phenotypes, have an established role in ciliogenesis. These macromolecular complexes ensure anterograde trafficking by ATP-dependent movement from the ciliary base toward the growing end of microtubules. In the context of kinesin-2 ablation, model organisms such as mouse or zebrafish display stunted or absent ciliary formation, leading to broad impairment of primary ciliary functions during vertebrate development.[2]

Protein synthesis does not occur in the cilium; the formation and maintenance of this organelle depends on

---

[1] CHU Nantes, Service de Génétique Médicale, 9 quai Moncousu, 44093 Nantes Cedex 1, France; [2] Université de Nantes, CNRS, INSERM, l'institut du thorax, 44000 Nantes, France; [3] Center for Human Disease Modeling, Duke University Medical Center, Durham, NC 27701, USA; [4] Department of Medical Genetics, Oslo University Hospital and University of Oslo, 0407 Oslo, Norway; [5] University of Paris, INSERM U1163, Institut Imagine, 75015 Paris, France; [6] The Institute for Genomic Medicine at Nationwide Children's Hospital, Columbus, OH 43205, USA; [7] Service d'Ophtalmologie, Hôtel Dieu, CHU de Nantes, 44093 Nantes, France; [8] Service de Pédiatrie, Hôpital Mère-Enfants, CHU de NANTES, 44093 Nantes, France; [9] Unité d'Hépatologie pédiatrique, Centre de référence de l'atrésie des voies biliaires et des cholestases génétiques Hôpital NECKER, 75015 Paris, France; [10] Human Genetics Center, School of Public Health, University of TX Health Science Center at Houston, Houston, TX 77030, USA; [11] Ruiz Department of Ophthalmology and Visual Science, University of TX Health Science Center at Houston, Houston, TX 77030, USA; [12] Ocular Genomics Institute, Massachusetts Eye and Ear Infirmary, Harvard Medical School, Boston, MA 02114, USA; [13] Jules Stein Eye Institute and Department of Ophthalmology, University of California Los Angeles, Los Angeles, CA 90095, USA; [14] Advanced Center for Translational and Genetic Medicine (ACT-GeM), Stanley Manne Children's Research Institute, Ann & Robert H. Lurie Children's Hospital of Chicago, Chicago, IL 60611, USA; [15] Department of Pediatrics, Feinberg School of Medicine, Northwestern University, Chicago, IL 60611, USA; [16] Department of Small Animal Clinical Studies, College of Veterinary Medicine, Michigan State University, East Lansing, MI 48824, USA; [17] Department of Veterinary Medicine and Surgery, College of Veterinary Medicine, University of Missouri, Columbia, MO 65211, USA; [18] Service de Génétique, Hôpital Necker-Enfants Malades, AP-HP, 75015 Paris, France

[19] These authors contributed equally to this work

[20] These authors contributed equally to this work

*Correspondence: eridavis@luriechildrens.org (E.E.D.), bertrand.isidor@chu-nantes.fr (B.I.)

https://doi.org/10.1016/j.ajhg.2020.04.005.

intraflagellar transport (IFT) of protein cargo along the ciliary axoneme. KIF3A-KIF3B or KIF3A-KIF3C heterodimers and the non-motor kinesin-associated protein (KAP), encoded by *KIFAP3*, operate as the main effectors of kinesin-2 driven trafficking, together with homodimeric KIF17. Ciliopathies, defined as clinical entities caused by defects in ciliary structure or function, share common phenotypic features; these include obesity, hepatic fibrosis, retinitis pigmentosa (RP), cystic kidney disease, polydactyly, and intellectual disability.[3] Here, we report affected individuals from a small nuclear family and an unrelated six-generation pedigree whose members harbor heterozygous nonsynonymous *KIF3B* variants and share partially overlapping ciliopathy clinical features.

Individual 1 (family A, II-1; Table 1) is a male born from nonconsanguineous parents of northern European ancestry. At birth, postaxial hexadactyly of both hands and the right foot were observed. At 12 months, he presented with failure to thrive and hepatosplenomegaly. An abdominal ultrasound performed at 18 months showed a dysmorphic liver with dilatation of intrahepatic biliary ducts. A liver biopsy showed micronodular cirrhosis with modification of global hepatic architecture by annular fibrosis and persistence of peripheric biliary neoductules. Cardiac ultrasound showed a bicuspid aortic valve. At 24 months of age, he had esophageal varices and thrombocytopenia. At 4 years of age, because of suggestive clinical features of a ciliopathy, we performed an ophthalmological exam. The parents only reported their child to have difficulties moving at night. Fundus examination was normal (Figure 1Aa), but the fundus autofluorescence showed a modification of the peripheral autofluorescence and hyperautofluorescent perimacular points (Figure 1Ab). Electroretinograms showed alteration of the flicker and the scotopic responses (Figure S1). Spectral Domain Optical Coherence Tomography (SD-OCT) analysis showed a normal foveal profile (Figure 1Ac,d). At last ophthalmological examination at the age of 5 years, fundus examination showed retinal thinning with an increase in the visibility of the choroidal vascularization on the retinal periphery and on the temporal macula.

To investigate the genetic etiology of this individual's clinical presentation, we consented the parent-child trio for all subsequent research procedures in accordance with ethical guidelines of Nantes University Hospital (Figure 2A). Array comparative genomic hybridization on the family A proband sample was negative, ruling out the possibility of large copy number variants. Next, we performed exome sequencing of the proband and achieved an average mean target coverage of 86× (Supplemental Methods). We retained variants with at least 9 reads and with a variant read frequency over 20% impacting exonic sequences or splice sites (±10 bp from the junction) and with an allele frequency <0.5% in 1000 Genomes, Genome Aggregation Database (gnomAD, 123,136 exomes and 15,496 whole-genome sequences; accessed on 11/10/2018), and in a local database of 952 exomes. We retained 280 rare variants (Table S1), including 13 that matched an X-linked or a recessive inheritance (homozygous, hemizygous, or at least 2 rare variants in the same gene) and 267 that matched a dominant inheritance (single heterozygous variant). We did not identify deleterious variants in any disease-associated gene, and we selected 88 variants of uncertain significance that were within an established human genetic disease-associated gene in either OMIM or Orphanet for further consideration (Table S1).

The constellation of clinical phenotypes observed in individual 1 was suggestive of a ciliary disorder. We therefore overlaid the rare exome-sequencing variant set with 303 ciliary genes from the SYSCILIA Gold Standard (SCGSv.1).[4] We identified five rare heterozygous nonsynonymous variants that intersected with the SCGSv.1 dataset (Table S1). Five variants were heterozygous alleles in genes already causally implicated in recessive ciliopathies. However, one variant in *KIF3B* (GenBank: NM_004798.4, c.748G>C [p.Glu250Gln]) was absent from gnomAD and predicted to be deleterious by SIFT,[5] PolyPhen-2,[6] and MutationTaster.[7] Given the important role of KIF3B in anterograde IFT in cilia, and localization of this variant to the conserved kinesin motor domain (Figures 2B, 2C, S2, and S3), we tested familial segregation by Sanger sequencing and confirmed that the variant was *de novo*. We excluded false paternity and maternity by analysis of 11 microsatellite markers.

Through the data sharing platform GeneMatcher,[8] we became aware of another rare *KIF3B* variant that had been identified as a possible cause of RP. This second variant (GenBank: NM_004798.4, c.1568T>C [p.Leu523Pro]) was found in two samples from a cohort of more than 200 families with autosomal-dominant RP ascertained in an ongoing study at the University of Texas Health Science Center in Houston.[9] The two females were originally thought to be unrelated but the identification of rare variants during exome sequencing led to the eventual discovery that they were cousins (family B: IV-4 and V-4; Figure 2A; Table 1; Supplemental Methods). They are part of an extended Ashkenazi Jewish family that has RP segregating through at least six generations with more than 19 affected individuals reported (Figure 2A). There is no evidence of consanguinity in either branch of the family and male-to-male transmission of the disease excludes an X-linked mode of inheritance.

Affected members of family B exhibit classic symptoms of RP, with an average age of onset in the first decade. We performed detailed clinical assessment for five individuals (IV-1, IV-3, V-4, VI-2, and VI-1 [individuals 2–6]; Table 1; Figure 1B). Two members of the family have postaxial polydactyly (IV-8 and V-7), and one individual is reported to have kidney dysfunction (V-I; Table 1). Given their symptoms evocative of a ciliopathy, targeted genetic testing had been done previously on known genes for Bardet-Biedl syndrome (MIM: 209900) and dominant forms of inherited retinal degeneration.

Table 1. Clinical Summary of Individuals Harboring Nonsynonymous *KIF3B* Variants

	Family A	Family B				
Center	Nantes (France)	Houston (USA)				
Individual identifier	1	2	3	4	5	6
Affected individual	II-1	IV-1	IV-3	V-4	VI-2	VI-1
Gender	male	male	male	female	female	male
Age at last examination (years)	5	50	55	52	23	21
Eye	retinitis pigmentosa	retinitis pigmentosa	retinitis pigmentosa	retinitis pigmentosa	retinitis pigmentosa	retinitis pigmentosa
Eye: visual field area (OS;OD) [degrees diameter]	N/D	10; 10	20; 22	ND	20 OU	constricted central vision
Eye: age of first visual symptoms	diagnosed at 5 years	6 years	diagnosed at 5 years	unknown	unknown	reports symptoms to be more severe than mother (V-4) or sister (VI-2)
Liver	hepatic fibrosis	normal	normal	normal	normal	normal
Skeletal malformations	postaxial hexadactyly of both hands and right foot	normal	normal	affected mother (IV-8) and affected brother (V-7) both reported to have postaxial hexadactyly	normal	normal
Heart	bicuspid aortic valve	normal	normal	normal	normal	normal
Kidney	normal	son (V-1) has kidney issues (dialysis)	normal	normal	normal	normal

Abbreviations are as follows: N/D, no data; OS, oculus sinister (left eye); OD, oculus dexter (right eye); OU, oculus uterque (both eyes).

No likely pathogenic variants were identified, leading to additional testing by exome sequencing.

Bioinformatic analysis of exome data from family B was done using MendelScan as described,[10] resulting in 28 rare variants shared between both individuals (Table S2). The majority of shared variants were present in multiple individuals in gnomAD, especially Ashkenazi Jewish ($n = 23$ variants with allele frequency $> 0.05\%$; 50,040 individuals). The *KIF3B* variant was the only segregating variant absent in gnomAD. We performed segregation analysis of the four variants with the lowest overall incidence in gnomAD (*KIF3B*, *PCNXL3*, *OR4D2*, and *TOB1*) in an additional seven family members from the extended pedigree using bidirectional Sanger sequencing (six affected, one unaffected; Figure 2A). The *KIF3B* c.1568T>C (p.Leu523Pro) variant was the sole change that segregated with RP in the pedigree. To confirm that the *KIF3B* variant and the disease are not likely to be co-segregating by chance, we calculated a LOD score (logarithm of the odds) for the 14 informative meioses observed across the extended family. The LOD score of 4.2 (odds ratio 16,384:1) is strong statistical evidence supporting the *KIF3B* change as the cause of disease in the family. p.Leu523Pro is located in the coiled coil domain of KIF3B at a position conserved throughout vertebrates (Figures 2B, 2C, S2, and S3) is predicted to be pathogenic by SIFT,[5] PolyPhen-2,[6] and MutationTaster[7] and is absent from all available databases, including gnomAD.

To characterize the cellular phenotypes induced by the dominantly inherited *KIF3B* variants identified in humans, we evaluated primary cilia length in skin fibroblasts isolated from individual 1 (family A; Supplemental Methods). We cultured fibroblasts under standard protocols of serum deprivation for 24 h to promote primary cilium elongation.[11–13] We fixed case- and age-matched control cells and immunolabeled γ-tubulin and ARL13b as markers of the basal body and ciliary axoneme, respectively (Figure 3A; Table S3). We first noted that the proportion of ciliated cells from individual 1 was similar to those from the age-matched control ($>90\%$; $n = 66/72$ and $n = 147/153$ fibroblasts/condition isolated from age-matched control and individual 1, respectively; Figure 3B). Next, we found that the primary cilia length was increased significantly in fibroblasts from individual 1 compared to age-matched control fibroblasts (36% average increase in case versus control cilia; $p < 0.0001$; Figure 3C).

To validate the cilia length abnormalities observed in primary fibroblasts from individual 1, we evaluated the effect of *KIF3B* variants from both families in a ciliated context using hTERT-RPE1 cells, a commonly used immortalized retinal pigment epithelial cell line. We transfected C-terminally myc-tagged vectors encoding either WT or variant *KIF3B* (p.Glu250Gln; p.Leu523Pro or p.Val435Ile [negative control, rs41288638; 230/276,748 alleles in gnomAD]), fixed cells at 24 h post-transfection, performed

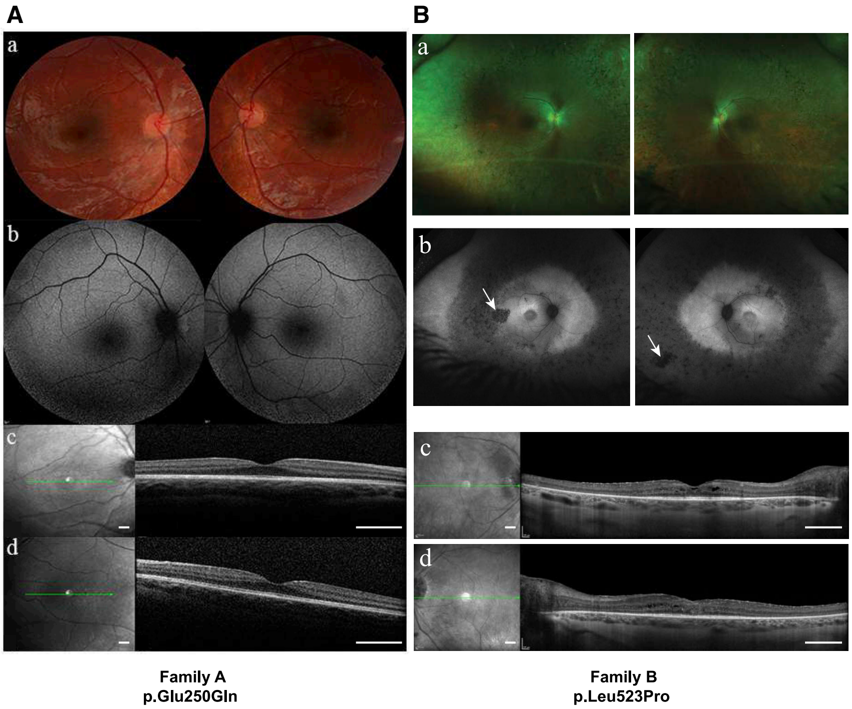

Figure 1. Individuals Harboring Nonsynonymous *KIF3B* Variants Display Retinal Phenotypes

(A) Ophthalmological examination of individual 1 (family A) who harbors a *de novo* c.748G>C (p.Glu250Gln) *KIF3B* variant. Shown are (a) ophthalmological fundus imaging of the right and the left eyes; (b) fundus autofluorescence imaging of the right and the left eyes; (c) spectral domain optical tomography of the right fovea (scale: 1 mm); and (d) spectral domain optical tomography of the left fovea (scale: 1 mm). Refraction was performed under cycloplegia with chlorhydrate of cyclopentolate 0.5% (Alcon). Optical coherence tomography (OCT) analysis and the autofluorescence fundus imaging were conducted with an OCT spectral domain (Heidelberg Engineering, Spectralis HRA-OCT).
(B) Ophthalmological examination of individual VI-2 (family B) who harbors a c.1569T>C (p.Leu523Pro) *KIF3B* variant. White arrows indicate retinal pigments characteristic of retinitis pigmentosa. Shown are (a) ophthalmological fundus imaging of the right and the left eyes; (b) fundus autofluorescence imaging of the right and the left eyes; (c) spectral domain optical tomography of the right fovea (scale: 1 mm); and (d) spectral domain optical tomography of the left fovea (scale: 1 mm).

immunostaining with γ-tubulin and ARL13B, and measured cilia length (Supplemental Methods; Tables S3 and S4). We observed no significant differences in primary cilia length between cells transfected with empty vector, *KIF3B-WT-myc*, or *KIF3B-p.Val435Ile-myc* constructs (Figures 3D and 3E). However, we detected a significant increase in primary cilia length for both case-associated variants compared to WT KIF3B (9% increase in p.Glu250Gln cells versus control, $p < 0.01$; and 13% increase in p.Leu523Pro cells versus control, $p < 0.0001$; Figures 3D and 3E). Notably, immunoblotting of myc-tag in whole-cell protein lysates isolated from transiently transfected HEK293 cells expressing KIF3B-myc variant constructs showed no significant differences in KIF3B protein levels compared to the *KIF3B-WT-myc* transfected condition (Supplemental Methods; Figure S4; Table S3).

To investigate further the stability of KIF3B protein harboring p.Glu250Gln or p.Leu523Pro, we monitored protein levels in a time course study after exposure to a protein synthesis inhibitor (Supplemental Methods; Table S3). We transiently transfected HEK293 cells with control and mutant *KIF3B-myc* constructs and treated cells with cycloheximide (50 μm for 2 and 4 h before protein harvest). Consistent with our initial results (Figure S4), we found no significant difference in KIF3B-myc protein levels across conditions exposed to cycloheximide for up to 4 h (Figures 3F–3J). These data support the notion that KIF3B protein harboring p.Glu250Gln or p.Leu523Pro do not undergo rapid degradation. Together, the cilia length and protein stability data indicate that primary cilia are markedly altered in the context of both KIF3B p.Glu250Gln and p.Leu523Pro variants but not for the KIF3B p.Val435Ile variant, supporting the specificity of this organellar defect.

To establish further a functional link between altered ciliary structure and overlapping human phenotypes observed in individuals with *KIF3B* variants, we considered prior knowledge from *in vivo* models of KIF3B dysfunction. *Kif3b* mouse models harboring a gene-trapped locus deleting a portion of exon 1 are embryonic lethal in homozygosity.[14–16] A *Cre*-loxP conditional knockout mouse showed that loss of *Kif3b* results in a rapid photoreceptor degeneration associated with opsin mislocalization to rod inner segments, but $Kif3b^{-/+}$ animals are viable and display no detectable retinal phenotypes.[17] Additionally, $kif3b^{-/-}$ zebrafish models carrying a GenBank: NM_001100145.1; c.1105C>T (p.Gln369*) encoding mutation display either absent or significantly reduced cilia length in multiple tissue types,[18] contrary to our observations from *KIF3B* mutant primary fibroblasts with elongated cilia (Figures 3A and 3B).

Moreover, as part of ongoing work to identify the molecular basis of clinically relevant traits in the domestic cat, we identified a nonsynonymous *KIF3B* change, ENSFCAT00000022266; c.1000G>A (p.Ala334Thr), as the likely cause of a recessive progressive retinal atrophy in the Bengal cat[19] (Supplemental Note). We performed a genome-wide association study on 98 Bengal cats to localize an associated region on cat chromosome A3 (Supplemental Methods; Figure 4A; Table S5) and overlaid these data with whole-genome sequencing data from a trio of cats

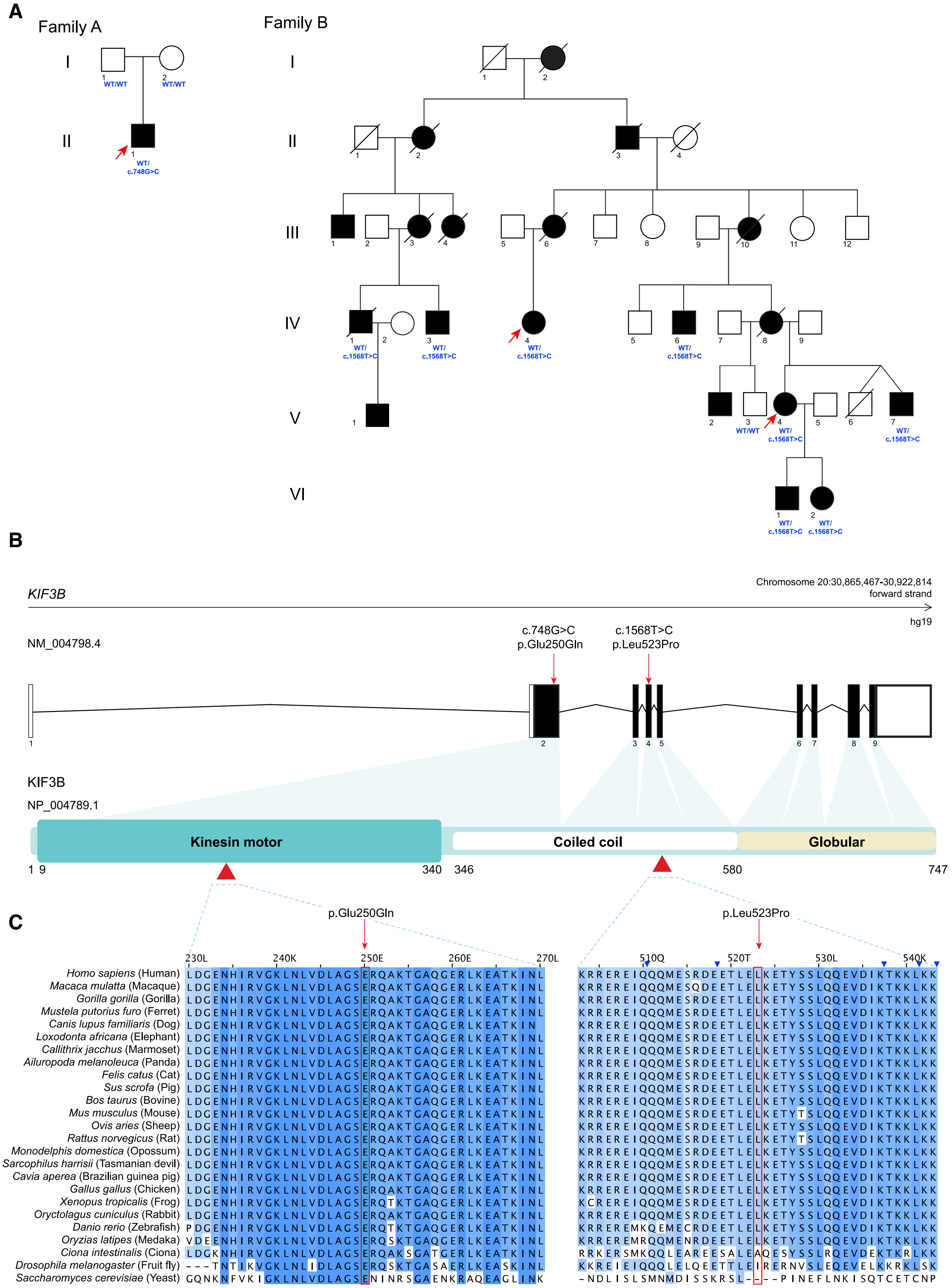

Figure 2. Heterozygous Nonsynonymous Variants in *KIF3B* Segregate with Ciliopathy Phenotypes in Dominant Pedigrees

(A) Pedigrees of families A and B with segregation of *KIF3B* variants. Filled circles and squares represent affected female or male individuals, respectively; unfilled circles and squares represent unaffected female or male individuals; respectively. Deceased individuals are indicated by diagonal lines. Exome sequencing was performed for individuals marked with an arrow. Individual genotypes at the *KIF3B* locus are indicated in blue. All affected individuals in family B carried the *KIF3B* c.1568T>C (p.Leu523Pro) encoding variant (IV-1, IV-3, IV-4, IV-6, V-4, V-7, VI-1, VI-2) but the unaffected individual (V-3) was WT.

(B) Schematic of *KIF3B* gene organization and protein domains. Untranslated exons, white boxes; translated exons, black boxes; red arrows and arrowheads, *KIF3B* variants identified in humans. Kinesin motor, coiled coil, and globular domains (UniProtKB, PROSITE annotations, GenBank: NP_004789.1) are indicated.

(legend continued on next page)

from the Bengal research colony (Table S6). The *KIF3B* p.Ala334Thr-encoding change was the sole variant that segregated with disease and is predicted to impair the kinesin motor domain (Figure S5). Importantly, we observed rhodopsin mislocalization to photoreceptor inner segments in $KIF3B^{-/-}$ mutant kittens as early as 8 weeks of age, consistent with structural and functional photoreceptor degeneration[19] (Figure 4B; Supplemental Note; Supplemental Methods). Together, our *in vitro* data and *in vivo* observations from recessive *KIF3B* vertebrate models argue against a haploinsufficiency model for the affected humans in our study.

To pursue the possibility of a dominant pathogenic effect for the p.Glu250Gln and p.Leu523Pro changes, we introduced mutant mRNAs into the developing zebrafish (Supplemental Methods; Table S4). The zebrafish genome encodes a single *KIF3B* ortholog (GRcZ11), for which the encoded protein (GenBank: NP_001093615.1) has 78% identity and 87% similarity to that of human (GenBank: NP_004789.1). Importantly, ablation of each of *kif3b* and its cognate kinesin-2 effectors encoded by *kif3a* and *kif3c* have been characterized previously in the zebrafish retina and perform similar trafficking functions to mammalian counterparts.[18] We and others have shown that alteration of numerous genes involved in retinal degeneration can give rise to microphthalmia in zebrafish.[20–22] As an initial test of the impact of either missense change on KIF3B function, we injected 100 pg WT or mutant *KIF3B* mRNA into embryos at the one-to-four cell stage and evaluated them live at 3 days post-fertilization (dpf) for external optic area in lateral bright field images using automated imaging and image analysis platforms (Supplemental Methods). We found no significant differences in eye size for clutches injected with p.Leu523Pro- or p.Val435Ile-encoding mRNA versus either WT or uninjected controls (Figures S6A and S6B). However, we observed marked lethality induced by p.Glu250Gln and assessed the effects of progressively decreasing amounts of mutant mRNA (50 pg, 25 pg, and 10 pg). The highest non-lethal doses resulted in a significant, dose-dependent, and reproducible reduction in eye area (19% reduction versus WT-injected at 50 pg; $p < 0.0001$; Figure S6C), an observation that persisted when normalized to larval body length to control for any possible developmental delay (Figure S6D). Co-injection of a 2:1 stoichiometric ratio of 100 pg WT with 50 pg p.Glu250Gln mRNA restored eye size to normal (not significantly different from equivalent doses of either WT or p.Glu250Gln alone; Figures S6A and S6B), supporting the specificity of p.Glu250Gln effect on eye morphology.

We hypothesized that the observed microphthalmia was caused by excessive cell death in the retina. In zebrafish and other vertebrates, the developing retina undergoes several waves of apoptosis that are necessary for the establishment of the retinal neuron networks. The first wave arises around 3 dpf and slows down at 5 dpf and the second wave takes place at 7 dpf.[23] We evaluated apoptosis in retinal sections at 5 dpf by counting terminal deoxynucleotidyl transferase dUTP nick-end labeling (TUNEL) positive cells (Supplemental Methods). We found no significant differences between larvae injected with either WT, p.Val435Ile-, or p.Leu523Pro-encoding mRNA compared to uninjected controls. However, we observed a modest but significant increase in apoptotic cells in larvae injected with p.Glu250Gln-encoding mRNA (50 pg; $p < 0.05$; Figures S7A and S7B), which is concordant with the microphthalmia phenotype observed in this condition (Figure S6).

In the zebrafish retina, Kif3b plays a role in photoreceptor formation and function through the connecting cilium that is specific to low light intensity (scotopic) detection facilitated by rod cells.[18] Further, *kif3b* mutants have documented defects in rhodopsin transport, consistent with other kinesin-2 mutants such as $kif3a^{-/-}$.[18] To determine whether zebrafish larvae with heterologous expression of mutant human *KIF3B* display defects in photoreceptor integrity, we evaluated rhodopsin localization in retinal sections at 5 dpf (Supplemental Methods; Table S3). We found no detectable differences between larvae injected with either WT or p.Val435Ile-encoding mRNA compared to uninjected controls (Figures 5A–5C). However, we observed a significant increase of rhodopsin in the rod inner segment for p.Leu523Pro (100 pg; $p < 0.001$), and to a greater extent, p.Glu250Gln-encoding (50 pg; $p < 0.0001$), versus WT mRNA (repeated with similar results, investigator masked to experimental condition; Figures 5A–5C). Consistent with the eye area studies, co-injection of 100 pg WT human *KIF3B* mRNA rescued the rhodopsin mislocalization defects of both variants such that they were indistinguishable from uninjected controls (Figures 5A and 5C)

We next wondered whether the observed rhodopsin mislocalization was coincident with altered cilia length in zebrafish with ectopic expression of *KIF3B* mutant mRNAs. To paint photoreceptor-connecting cilia, we performed antibody staining of transverse cryosections from 5 dpf larvae with two ciliary markers, acetylated α-tubulin and IFT52, and measured length of structures with double labeling (Supplemental Methods; Figure 5D; Table S3). We

(C) Conservation of 40 amino acid blocks impacted by nonsynonymous changes shown with a multiple sequence alignment (Clustal W v1.81) of 25 species sorted by pairwise identity. Red boxes, variant residues; blue shading of amino acids from dark to light represents most to least conserved, respectively. UniProtKB identifiers: *Homo sapiens*, O15066; *Macaca mulatta*, F6S877; *Gorilla gorilla*, G3RAF7; *Mustela putorius furo*, M3Z2F0; *Canis lupus familiaris*, E2QUS2; *Loxodonta africana*, G3T0G8; *Callithrix jacchus*, F7IBN6; *Ailuropoda melanoleuca*, G1M429; *Felis catus*, A0A2I2UKW2; *Sus scrofa*, F1S519; *Bos taurus*, F1N020; *Mus musculus*, Q61771; *Ovis aries*, W5NZV7; *Rattus norvegicus*, D3ZI07; *Monodelphis domestica*, F6RWN1; *Sarcophilus harrisii*, G3WA27; *Cavia aperea*, ENSCAPP00000010080 (ensembl, UniProtKB identifier not available); *Gallus gallus*, Q5F423; *Xenopus tropicalis*, F6R640; *Oryctolagus cuniculus*, G1U1D0; *Danio rerio*, F1QN54; *Oryzias latipes*, H2LAE9; *Ciona intestinalis*, F7B875; *Drosophila melanogaster*, P46867; *Saccharomyces cerevisiae*, P28742.

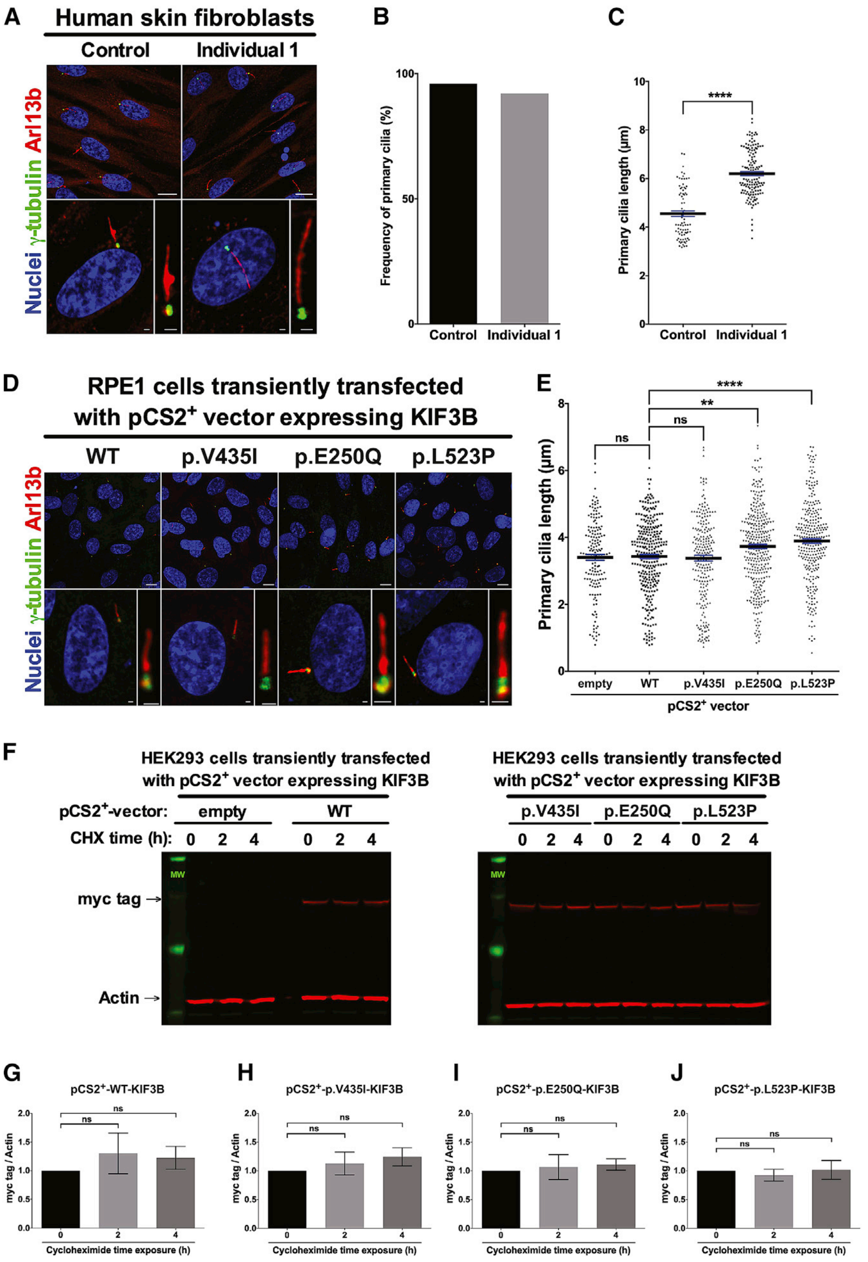

Figure 3. *KIF3B* p.Glu250Gln and p.Leu523Pro Variants Increase Primary Cilia Length

(A) Representative confocal images of primary human fibroblasts from the family A proband. Cells were methanol-fixed and immunostained with anti-ARL13b rabbit polyclonal antibody (red) and anti-γ-tubulin mouse IgG1 monoclonal antibody (green) and mounted with DAPI-Fluoromount G (blue) as markers of the primary cilium, basal body, and nuclei, respectively. Scale bars: 10 μm (top row) and 1 μm (bottom row). See Table S3 for details about antibodies used.

(B) Frequency of ciliated cells in primary skin fibroblasts from individual 1 (family A) and a matched control subject.

(C) Quantification of the primary cilia length measured on cells from a matched human control (4.55 ± 0.11 μm, n = 82) and individual 1 (family A) primary fibroblasts (6.20 ± 0.08 μm, n = 141).

For (B) and (C), six random images were assessed for each of control and affected; two independent replicates.

(D) Representative confocal images of hTERT-RPE1 cells transiently transfected with pCS2$^+$-*KIF3B-myc* vectors and immunostained with anti-ARL13b (red) and anti-γ-tubulin (green) and mounted with DAPI-Fluoromount G as markers of the primary cilium, basal body, and nuclei, respectively. Scale bars: 10 μm (top row) and 1 μm (bottom row).

(E) Quantification of primary cilia length of hTERT-RPE1 cells transiently transfected with pCS2$^+$-empty (3.40 ± 0.09 μm, n = 166), pCS2$^+$-*KIF3B-WT-myc* (3.43 ± 0.06 μm, n = 302), pCS2$^+$-*KIF3B-p.V435I-myc* (3.38 ± 0.09 μm, n = 233), pCS2$^+$-*KIF3B-p.E250Q-myc* (3.73 ± 0.07 μm, n = 341), and pCS2$^+$-*KIF3B-p.L523P-myc* (3.89 ± 0.07 μm, n = 303) vectors. Data are collected from six independent replicate experiments.

(F) Western blot analysis of myc tag (KIF3B protein levels) and actin in HEK293 cells transiently transfected with pCS2$^+$-*KIF3B-myc* vectors and exposed 48 h post transfection to 50 μM cycloheximide for 0, 2, and 4 h.

(G–J) Quantitative analysis of immunoblotting results shown in (F); myc tag (KIF3B protein levels) was normalized to actin in transiently transfected HEK293 cells and data are shown relative to pCS2$^+$-*KIF3B-WT-myc* vector. Performed in biological triplicates.

Data in all panels represent mean ± SEM. Statistical comparisons were performed with two-tailed unpaired t test (GraphPad PRISM software). ns, not significant, $^{**}p < 0.01$; $^{****}p < 0.0001$.

found no significant differences in connecting cilium length between larvae injected with either WT or p.Val435Ile encoding mRNA compared to uninjected controls (Figures 5E and 5F). However, we observed a significant elongation of connecting cilia for p.Leu523Pro-encoding (100 pg; $p < 0.0001$) and p.Glu250Gln-encoding (50 pg; $p < 0.0001$) versus WT mRNA (repeated with similar results; Figures 5E and 5F). We detected no differences in length measurements when acetylated α-tubulin and IFT52 signal was assessed individually, arguing against sequestration of IFT-B components as the molecular mechanism underpinning the long cilia phenotype (Figure S8). In aggregate, these data reinforce the relevance of *KIF3B* function to photoreceptor integrity and opsin trafficking in rod photoreceptors and support the pathogenicity of p.Glu250Gln and p.Leu523Pro.

The molecular motor is essential for kinesin complexes to move along microtubules in an ATP-dependent manner[24] and multiple dominant pathogenic amino acid substitutions in kinesin genes have been identified in this domain. The Glu250 position is an ultra-conserved residue in 41/42 human kinesin motor domain protein

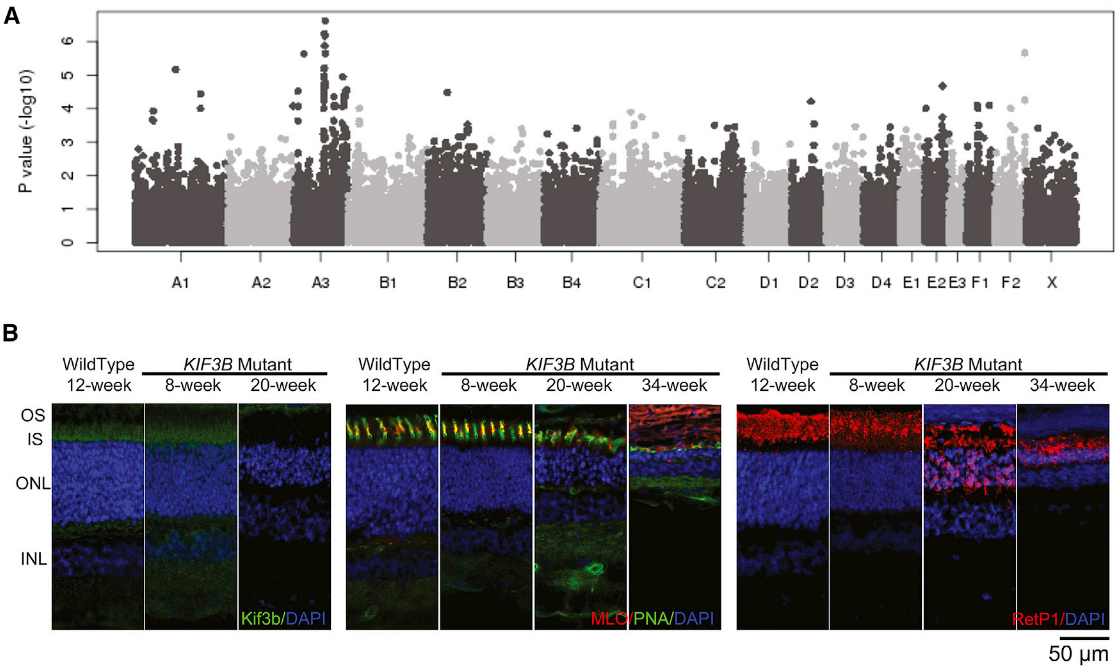

Figure 4. A Recessive c.1000G>A (p.Ala334Thr) Mutation in *KIF3B* Is a Likely Cause for Progressive Retinal Atrophy in Bengal Cats
(A) Manhattan plot of GWAS for cat progressive retinal atrophy. After Bonferroni correction, several SNPs on cat chromosome A3 suggest a significant association with Bengal cat progressive retinal atrophy (Table S5). Cat chromosome A3 has genes homologous to human chromosome 20.
(B) Morphological and cellular changes as analyzed by immunohistochemistry. Left panel, anti-Kif3b antibody labels the region of the photoreceptor inner segment (IS) in wild-type cats. Similar labeling was detectable in sections from 8-week-old *KIF3B* homozygous mutants, but not in sections from 20-week-old mutant kittens. See Table S3 for details of antibodies used. Central panel, combination staining of the cone markers peanut agglutinin (PNA; cone sheath) with cone ML opsin (MLO). Cone morphology in *KIF3B* mutants at 8 weeks appears relatively normal but by 20 weeks there was distortion and stunting of outer segments with reduced ML opsin labeling. By 34 weeks of age, only short residual PNA labeling material remained with reduced ML opsin labeling. The outer nuclear layer (ONL) was progressively thinned. Right panel, labeling with a rhodopsin marker (RetP1). Rhodopsin is mislocalized in mutants to the inner segment as early as 8 weeks of age, then mislocalized to the outer nuclear layer cells bodies and synaptic terminals by 20 weeks. The rod inner and outer segments (OS) also showed some degeneration with disease progression.

sequences, except KIF26B (Figure S2) and vertebrate KIF3B orthologs (Figure 2C). This residue was substituted by a lysine in *KIF1A* (GenBank: NM_001244008.1; c.757G>A [p.Glu253Lys]) in two individuals with neuroanatomical phenotypes described by Lee et al.[24] Notably, individuals carrying this variant exhibited a severe phenotype, consistent with the more acute presentation of individual 1 (family A) in our study. Five case subjects with substitutions of the equivalent residue in *KIF5C* by a Lys or Val were also reported.[25] Rice et al. observed that when the glutamic acid was substituted by alanine (p.Glu236Ala), the ATPase activity of the kinesin was reduced at least 1,000-fold.[26] Hence, this variant might act in a dominant manner by altering the ability of the KIF3A/B heterodimer to move along the ciliary microtubules, disorganizing ciliogenesis and thus causing the augmented primary cilia length of the fibroblasts of individual 1 (Figure 3).

Kittens homozygous for the *KIF3B* mutation showed a rapid loss of photoreceptors. KIF3B immunolabeling showed that initially the mutant protein was detectable in the region of inner and outer segments; however, with progressive degeneration of both layers and loss of photoreceptor nuclei Kif3b immunoreactivity was no longer detectable (Figure 4B). This loss of immunoreactivity was accompanied by pronounced mislocalization of rhodopsin. Abnormal trafficking of opsin to the outer segment with retention in the inner segment and cell body has been reported in a number of retinal degeneration conditions including RP in humans and animal models.[27–33] The *KIF3B* p.Ala334Thr variant in the Bengal cat might not totally ablate protein function resulting in a recessive retinal phenotype, in contrast to previously reported zebrafish and mouse recessive *KIF3B* mutants that are embryonic lethal.[14–16,18,34] Further studies are required to investigate impact of p.Ala334Thr on cilia length and KIF3B protein stability in the feline retina.

The ciliopathies are known for exhibiting variable expressivity of endophenotypes,[35] and this phenomenon is exemplified by the two pedigrees in our study and the Bengal cat. Inter- and intra-familial variability within this disease spectrum has been attributed to allelism at the same locus,[36] second-site modification in *trans*,[37] and for dominant disorders, variable expression of the wild-type allele.[38] Two different KIF3B protein domains are impacted by each of the deleterious variants characterized by this study (kinesin motor, family A versus coiled coil domain,

]

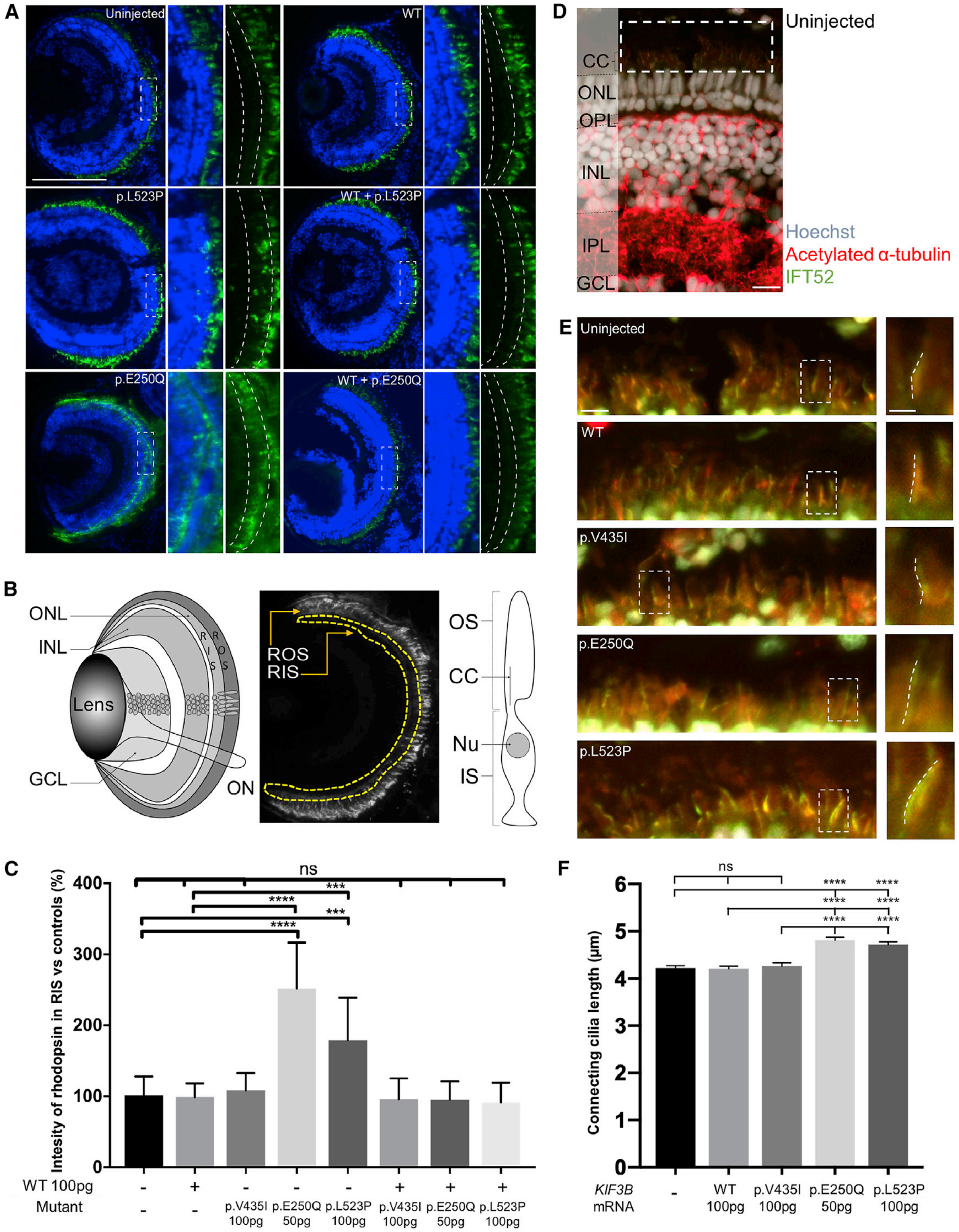

Figure 5. Retinal Phenotypes in Zebrafish Larvae with Heterologous Mutant *KIF3B* Expression

(A) Representative images of optic sections obtained from 5 dpf larvae and immunostained with anti-rhodopsin mouse monoclonal antibody (green) and Hoechst stain (blue). Dashed boxes indicate insets (right; with and without Hoescht). Dashed curved lines in insets demarcate rod inner segment (RIS). Scale bar: 50 μm, with equivalent scaling for each condition.

(B) Schematic of the zebrafish larval eye (left). GCL, ganglion cell layer; INL, inner nuclear layer; ONL, outer nuclear layer; ON, optic nerve. Schematic to indicate measurement of rhodopsin intensity in RIS of optic sections obtained from 5 dpf larvae (center). Area of interest is within yellow dashed lines; ROS, rod outer segment. Schematic of a rod photoreceptor (right). IS, inner segment; OS, outer segment.

(C) Quantification of rhodopsin intensity of RIS in optic sections (A and B) normalized to controls in 5 dpf larvae. n = 10 larvae per condition, repeated twice with similar results. Error bars indicate standard deviation (SD) of the mean.

(D) Representative merged image of an optic section obtained from a 5 dpf uninjected larva that was immunostained with anti-acetylated α-tubulin mouse monoclonal antibody (red, ciliary axoneme), anti-IFT52 rabbit polyclonal antibody (green, anterograde IFT), and

(legend continued on next page)

family B), leading us to speculate that allele effect could be sufficient to drive phenotype differences between the two families. Our *in vivo* assessment of rhodopsin trafficking in the zebrafish retina supports this posit (Figure 5). However, we cannot exclude the possibility that the family A proband has an exacerbated syndromic phenotype due to genetic interaction with additional variation in other loci that interact either directly or indirectly with *KIF3B*. We recognize that a limitation of this study is the fact that only coding regions were queried for variation; whole-genome sequencing will be required to obtain a complete list of contributory sites that determine phenotype in both families.

In conclusion, our study adds to the repertoire of ciliary genes that result in human pathology and characterize at clinical and molecular levels a ciliopathy hallmarked by RP, polydactyly, and liver fibrosis likely caused by an alteration of kinesin-2-driven transport. Most ciliopathies, especially those caused by IFT motor or raft proteins, are autosomal-recessive disorders.[39–41] However, we add another exception to this paradigm by reporting humans who harbor dominant *de novo* or inherited heterozygous variants, placing them in the class of dominant ciliopathies inclusive of conditions such as polycystic kidney disease (MIM: 173900) and orofacial digital syndrome (MIM: 311200).

Supplemental Data

Supplemental Data can be found online at https://doi.org/10.1016/j.ajhg.2020.04.005.

Acknowledgments

We are grateful to the families who participated in this study. We thank Kevin Adams, Westley Heydeck, and Julien Philippe for technical support and advice. We thank Brian Perkins for the IFT52 antibody, and his assistance with zebrafish antibody staining protocols. We also thank Stefan Scholz and Elisabet Teixido from UFZ as well as Tobias Kießling from "Scientific Software Solutions" (www.tks3.com) for use and assistance with FishInspector software. This work was supported by US National Institutes of Health grants HD042601 (N.K.), GM121317 (N.K.), DK072301 (N.K. and E.E.D.), and EY007142 (S.P.D.), and by grants from the Foundation Fighting Blindness USA (S.P.D.) and the William Stamps Farish Fund (S.P.D.). N.K. is a Distinguished Valerie and George D. Kennedy Professor. This project was funded in part previously by the National Center for Research Resources R24 RR016094 and the Office of Research Infrastructure Programs OD R24OD010928, the Phyllis and George Miller Feline Health Fund, Center for Companion Animal Health, School of Veterinary Medicine, University of California – Davis (2007-38-FM, 2008-08-F), the Winn Feline Foundation (MT07-012, W12-022), and Cat Health Network (D12FE-509) and the University of Missouri, College of Veterinary Medicine Gilbreath McLorn Endowment (L.A.L.). We appreciate the dedicated assistance of Bengal cat breeders for their participation in the research. S.M.P.-J. is funded by the Myers-Dunlap Endowment at Michigan State University. This work was supported by grants from the National Eye Institute (R01EY012910 to E.A.P., R01EY026904 to K.B. and E.A.P., and P30EY014104 for MEEI core support) and the Foundation Fighting Blindness (EGI-GE-1218-0753-UCSD to K.B. and E.A.P.).

Declaration of Interests

N.K. is a paid consultant for and holds significant stock of Rescindo Therapeutics, Inc.

Received: November 20, 2018
Accepted: April 2, 2020
Published: May 7, 2020

Web Resources

99 Lives Cat Genome Sequencing Initiative, http://felinegenetics.missouri.edu/99lives
1000 Genomes, http://www.internationalgenome.org/
ClustalW, http://www.clustal.org/
dbSNP, https://www.ncbi.nlm.nih.gov/projects/SNP/
Ensembl Genome Browser, http://www.ensembl.org/index.html
ExAC Browser, http://exac.broadinstitute.org/
Fiji, https://fiji.sc/
GenBank, https://www.ncbi.nlm.nih.gov/genbank/
GeneMatcher, https://genematcher.org/
gnomAD Browser, https://gnomad.broadinstitute.org/
NHLBI Exome Sequencing Project (ESP) Exome Variant Server, http://evs.gs.washington.edu/EVS/
OMIM, https://www.omim.org/
Orphanet, https://www.orpha.net/consor/cgi-bin/index.php
PLINK, http://pngu.mgh.harvard.edu/~purcell/plink/
QuickChange, http://www.genomics.agilent.com/primerDesignProgram.jsp
Syscilia, http://www.syscilia.org/goldstandard.shtml
UCSC Genome Browser, http://genome.ucsc.edu
UCSF Chimera software, https://www.cgl.ucsf.edu/chimera/
UniProt, http://www.uniprot.org/

Hoechst staining (gray; nuclei). CC, connecting cilium; OPL, outer plexiform layer; IPL, inner plexiform layer. Scale bar, 10 μm. Note that in addition to ciliary microtubules, anti-acetylated α-tubulin stains axon tracts throughout the retina.
(E) Left, representative magnified views with enhanced contrast to enable visualization of connecting cilia (equivalent across images; see dashed white box in D), scale bar: 5 μm, with equivalent scaling for each condition; right, insets show a magnified view of a representative connecting cilium (see dashed white box at left); dashed lines indicate ciliary length measurement, scale bar: 2 μm, with equivalent scaling for each condition.
(F) Quantification of photoreceptor connecting cilia length in 5 dpf retinas. $n = 10–12$ larvae per condition, $n = 174–246$ cilia per retina, repeated twice with similar results. Error bars indicate standard error of the mean (SEM).
Statistical comparisons were performed with a non-parametric one-way ANOVA followed by Tukey's multiple comparison (GraphPad PRISM software; v.7.0c). $^{****}p < 0.0001$, $^{***}p < 0.001$; ns, not significant; WT, wild type; p.Glu250Gln and p.Leu523Pro are variants identified in cases; p.Val435Ile is a negative control (rs41288638; 230/276,748 alleles in gnomAD). See Table S3 for antibodies used.

References

1. Reilly, M.L., Stokman, M.F., Magry, V., Jeanpierre, C., Alves, M., Paydar, M., Hellinga, J., Delous, M., Pouly, D., Failler, M., et al. (2019). Loss of function mutations in *KIF14* cause severe microcephaly and kidney development defects in humans and zebrafish. Hum. Mol. Genet. *28*, 778–795.
2. Goetz, S.C., and Anderson, K.V. (2010). The primary cilium: a signalling centre during vertebrate development. Nat. Rev. Genet. *11*, 331–344.
3. Badano, J.L., Mitsuma, N., Beales, P.L., and Katsanis, N. (2006). The ciliopathies: an emerging class of human genetic disorders. Annu. Rev. Genomics Hum. Genet. *7*, 125–148.
4. van Dam, T.J., Wheway, G., Slaats, G.G., Huynen, M.A., Giles, R.H.; and SYSCILIA Study Group (2013). The SYSCILIA gold standard (SCGSv1) of known ciliary components and its applications within a systems biology consortium. Cilia *2*, 7.
5. Kumar, P., Henikoff, S., and Ng, P.C. (2009). Predicting the effects of coding non-synonymous variants on protein function using the SIFT algorithm. Nat. Protoc. *4*, 1073–1081.
6. Adzhubei, I.A., Schmidt, S., Peshkin, L., Ramensky, V.E., Gerasimova, A., Bork, P., Kondrashov, A.S., and Sunyaev, S.R. (2010). A method and server for predicting damaging missense mutations. Nat. Methods *7*, 248–249.
7. Schwarz, J.M., Rödelsperger, C., Schuelke, M., and Seelow, D. (2010). MutationTaster evaluates disease-causing potential of sequence alterations. Nat. Methods *7*, 575–576.
8. Sobreira, N., Schiettecatte, F., Valle, D., and Hamosh, A. (2015). GeneMatcher: a matching tool for connecting investigators with an interest in the same gene. Hum. Mutat. *36*, 928–930.
9. Sullivan, L.S., Bowne, S.J., Birch, D.G., Hughbanks-Wheaton, D., Heckenlively, J.R., Lewis, R.A., Garcia, C.A., Ruiz, R.S., Blanton, S.H., Northrup, H., et al. (2006). Prevalence of disease-causing mutations in families with autosomal dominant retinitis pigmentosa: a screen of known genes in 200 families. Invest. Ophthalmol. Vis. Sci. *47*, 3052–3064.
10. Koboldt, D.C., Larson, D.E., Sullivan, L.S., Bowne, S.J., Steinberg, K.M., Churchill, J.D., Buhr, A.C., Nutter, N., Pierce, E.A., Blanton, S.H., et al. (2014). Exome-based mapping and variant prioritization for inherited Mendelian disorders. Am. J. Hum. Genet. *94*, 373–384.
11. Pampliega, O., Orhon, I., Patel, B., Sridhar, S., Díaz-Carretero, A., Beau, I., Codogno, P., Satir, B.H., Satir, P., and Cuervo, A.M. (2013). Functional interaction between autophagy and ciliogenesis. Nature *502*, 194–200.
12. Stoetzel, C., Bär, S., De Craene, J.-O., Scheidecker, S., Etard, C., Chicher, J., Reck, J.R., Perrault, I., Geoffroy, V., Chennen, K., et al. (2016). A mutation in VPS15 (PIK3R4) causes a ciliopathy and affects IFT20 release from the cis-Golgi. Nat. Commun. *7*, 13586.
13. Rozycki, M., Lodyga, M., Lam, J., Miranda, M.Z., Fátyol, K., Speight, P., and Kapus, A. (2014). The fate of the primary cilium during myofibroblast transition. Mol. Biol. Cell *25*, 643–657.
14. Nonaka, S., Tanaka, Y., Okada, Y., Takeda, S., Harada, A., Kanai, Y., Kido, M., and Hirokawa, N. (1998). Randomization of left-right asymmetry due to loss of nodal cilia generating leftward flow of extraembryonic fluid in mice lacking KIF3B motor protein. Cell *95*, 829–837.
15. Takeda, S., Yonekawa, Y., Tanaka, Y., Okada, Y., Nonaka, S., and Hirokawa, N. (1999). Left-right asymmetry and kinesin superfamily protein KIF3A: new insights in determination of laterality and mesoderm induction by kif3A-/- mice analysis. J. Cell Biol. *145*, 825–836.
16. Alsabban, A.H., Morikawa, M., Tanaka, Y., Takei, Y., and Hirokawa, N. (2020). Kinesin *Kif3b* mutation reduces NMDAR subunit NR2A trafficking and causes schizophrenia-like phenotypes in mice. EMBO J. *39*, e101090.
17. Jimeno, D., Lillo, C., Roberts, E.A., Goldstein, L.S.B., and Williams, D.S. (2006). Kinesin-2 and photoreceptor cell death: requirement of motor subunits. Exp. Eye Res. *82*, 351–353.
18. Zhao, C., Omori, Y., Brodowska, K., Kovach, P., and Malicki, J. (2012). Kinesin-2 family in vertebrate ciliogenesis. Proc. Natl. Acad. Sci. USA *109*, 2388–2393.
19. Ofri, R., Reilly, C.M., Maggs, D.J., Fitzgerald, P.G., Shilo-Benjamini, Y., Good, K.L., Grahn, R.A., Splawski, D.D., and Lyons, L.A. (2015). Characterization of an Early-Onset, Autosomal Recessive, Progressive Retinal Degeneration in Bengal Cats. Invest. Ophthalmol. Vis. Sci. *56*, 5299–5308.
20. Liu, Y.P., Bosch, D.G.M., Siemiatkowska, A.M., Rendtorff, N.D., Boonstra, F.N., Möller, C., Tranebjærg, L., Katsanis, N., and Cremers, F.P.M. (2017). Putative digenic inheritance of heterozygous RP1L1 and C2orf71 null mutations in syndromic retinal dystrophy. Ophthalmic Genet. *38*, 127–132.
21. Li, L., Nakaya, N., Chavali, V.R.M., Ma, Z., Jiao, X., Sieving, P.A., Riazuddin, S., Tomarev, S.I., Ayyagari, R., Riazuddin, S.A., and Hejtmancik, J.F. (2010). A mutation in ZNF513, a putative regulator of photoreceptor development, causes autosomal-recessive retinitis pigmentosa. Am. J. Hum. Genet. *87*, 400–409.
22. Shu, X., Zeng, Z., Gautier, P., Lennon, A., Gakovic, M., Cheetham, M.E., Patton, E.E., and Wright, A.F. (2011). Knockdown of the zebrafish ortholog of the retinitis pigmentosa 2 (RP2) gene results in retinal degeneration. Invest. Ophthalmol. Vis. Sci. *52*, 2960–2966.
23. Biehlmaier, O., Neuhauss, S.C., and Kohler, K. (2001). Onset and time course of apoptosis in the developing zebrafish retina. Cell Tissue Res. *306*, 199–207.
24. Lee, J.-R., Srour, M., Kim, D., Hamdan, F.F., Lim, S.-H., Brunel-Guitton, C., Décarie, J.-C., Rossignol, E., Mitchell, G.A., Schreiber, A., et al. (2015). De novo mutations in the motor domain of *KIF1A* cause cognitive impairment, spastic paraparesis, axonal neuropathy, and cerebellar atrophy. Hum. Mutat. *36*, 69–78.
25. Michels, S., Foss, K., Park, K., Golden-Grant, K., Saneto, R., Lopez, J., and Mirzaa, G.M. (2017). Mutations of *KIF5C* cause a neurodevelopmental disorder of infantile-onset epilepsy, absent language, and distinctive malformations of cortical development. Am. J. Med. Genet. A. *173*, 3127–3131.
26. Rice, S., Lin, A.W., Safer, D., Hart, C.L., Naber, N., Carragher, B.O., Cain, S.M., Pechatnikova, E., Wilson-Kubalek, E.M., Whittaker, M., et al. (1999). A structural change in the kinesin motor protein that drives motility. Nature *402*, 778–784.
27. Adamian, M., Pawlyk, B.S., Hong, D.-H., and Berson, E.L. (2006). Rod and cone opsin mislocalization in an autopsy eye from a carrier of X-linked retinitis pigmentosa with a Gly436Asp mutation in the RPGR gene. Am. J. Ophthalmol. *142*, 515–518.
28. Concepcion, F., and Chen, J. (2010). Q344ter mutation causes mislocalization of rhodopsin molecules that are catalytically

active: a mouse model of Q344ter-induced retinal degeneration. PLoS ONE *5*, e10904.

29. Gao, J., Cheon, K., Nusinowitz, S., Liu, Q., Bei, D., Atkins, K., Azimi, A., Daiger, S.P., Farber, D.B., Heckenlively, J.R., et al. (2002). Progressive photoreceptor degeneration, outer segment dysplasia, and rhodopsin mislocalization in mice with targeted disruption of the retinitis pigmentosa-1 (Rp1) gene. Proc. Natl. Acad. Sci. USA *99*, 5698–5703.
30. Nishimura, D.Y., Fath, M., Mullins, R.F., Searby, C., Andrews, M., Davis, R., Andorf, J.L., Mykytyn, K., Swiderski, R.E., Yang, B., et al. (2004). *Bbs2*-null mice have neurosensory deficits, a defect in social dominance, and retinopathy associated with mislocalization of rhodopsin. Proc. Natl. Acad. Sci. USA *101*, 16588–16593.
31. Mowat, F.M., Gornik, K.R., Dinculescu, A., Boye, S.L., Hauswirth, W.W., Petersen-Jones, S.M., and Bartoe, J.T. (2014). Tyrosine capsid-mutant AAV vectors for gene delivery to the canine retina from a subretinal or intravitreal approach. Gene Ther. *21*, 96–105.
32. Beltran, W.A., Cideciyan, A.V., Lewin, A.S., Iwabe, S., Khanna, H., Sumaroka, A., Chiodo, V.A., Fajardo, D.S., Román, A.J., Deng, W.-T., et al. (2012). Gene therapy rescues photoreceptor blindness in dogs and paves the way for treating human X-linked retinitis pigmentosa. Proc. Natl. Acad. Sci. USA *109*, 2132–2137.
33. Hollingsworth, T.J., and Gross, A.K. (2012). Defective trafficking of rhodopsin and its role in retinal degenerations. Int. Rev. Cell Mol. Biol. *293*, 1–44.
34. Feng, D., Chen, Z., Yang, K., Miao, S., Xu, B., Kang, Y., Xie, H., and Zhao, C. (2017). The cytoplasmic tail of rhodopsin triggers rapid rod degeneration in kinesin-2 mutants. J. Biol. Chem. *292*, 17375–17386.
35. Davis, E.E., and Katsanis, N. (2012). The ciliopathies: a transitional model into systems biology of human genetic disease. Curr. Opin. Genet. Dev. *22*, 290–303.
36. Braun, D.A., and Hildebrandt, F. (2017). Ciliopathies. Cold Spring Harb. Perspect. Biol. *9*.
37. Kousi, M., and Katsanis, N. (2015). Genetic modifiers and oligogenic inheritance. Cold Spring Harb. Perspect. Med. *5*, 5.
38. Rivolta, C., McGee, T.L., Rio Frio, T., Jensen, R.V., Berson, E.L., and Dryja, T.P. (2006). Variation in retinitis pigmentosa-11 (PRPF31 or RP11) gene expression between symptomatic and asymptomatic patients with dominant RP11 mutations. Hum. Mutat. *27*, 644–653.
39. Afzelius, B.A. (1976). A human syndrome caused by immotile cilia. Science *193*, 317–319.
40. Huynh Cong, E., Bizet, A.A., Boyer, O., Woerner, S., Gribouval, O., Filhol, E., Arrondel, C., Thomas, S., Silbermann, F., Canaud, G., et al. (2014). A homozygous missense mutation in the ciliary gene TTC21B causes familial FSGS. J. Am. Soc. Nephrol. *25*, 2435–2443.
41. Bujakowska, K.M., Zhang, Q., Siemiatkowska, A.M., Liu, Q., Place, E., Falk, M.J., Consugar, M., Lancelot, M.-E., Antonio, A., Lonjou, C., et al. (2015). Mutations in IFT172 cause isolated retinal degeneration and Bardet-Biedl syndrome. Hum. Mol. Genet. *24*, 230–242.

The American Journal of Human Genetics, Volume *106*

Supplemental Data

Mutations in the Kinesin-2 Motor *KIF3B* Cause an Autosomal-Dominant Ciliopathy

Benjamin Cogné, Xenia Latypova, Lokuliyanage Dona Samudita Senaratne, Ludovic Martin, Daniel C. Koboldt, Georgios Kellaris, Lorraine Fievet, Guylène Le Meur, Dominique Caldari, Dominique Debray, Mathilde Nizon, Eirik Frengen, Sara J. Bowne, 99 Lives Consortium, Elizabeth L. Cadena, Stephen P. Daiger, Kinga M. Bujakowska, Eric A. Pierce, Michael Gorin, Nicholas Katsanis, Stéphane Bézieau, Simon M. Petersen-Jones, Laurence M. Occelli, Leslie A. Lyons, Laurence Legeai-Mallet, Lori S. Sullivan, Erica E. Davis, and Bertrand Isidor

SUPPLEMENTARY INFORMATION

Supplementary Note. Recessive mutations in *KIF3B* cause retinal degeneration in Bengal cats.

As part of our ongoing work to identify the molecular underpinnings of clinically relevant traits in the domestic cat (*Felis silvestris catus*), we previously reported a recessively segregating progressive retinal atrophy (PRA) in the Bengal cat[1]. Mutant kittens show an early reduction in rod function and an early and progressive loss of outer retinal structure[1].

To determine the genetic change(s) responsible for this condition, we performed a genome-wide association study (GWAS) on 98 Bengal cats (44 cases and 54 controls) on the 63K feline SNP array (University of Missouri IACUC protocol 8313; Supplementary Methods). Bengal cats were originally donated, with written consent, by Bengal breeders for the establishment of a breeding colony. Cases and controls were either from Bengal cat owners or selected from the research colony[1]. All cases were confirmed by a board-certified veterinary ophthalmologist at the University of California-Davis Veterinary Medical Teaching Hospital or the MU Veterinary Health Center Ophthalmological Services. The genotyping rate was 0.99. Overall, 147 SNPs failed the missingness test (GENO > 0.2), 15,986 SNPs failed the frequency test (MAF < 0.05), leaving 46,821 SNPs for the GWAS. The GWAS indicated several SNPs in high association with the blindness phenotype on cat chromosome A3 (Table S5, Figure 3A). Several SNPs were significant in several regions of cat chromosome A3, suggesting assembly errors.

To delineate further the genetic cause of progressive retinal atrophy in these Bengal cats, we performed whole genome sequencing, as part of the 99 Lives Cat Genome Sequencing Initiative (Accession: PRJNA308208; BioProject PRJNA343385; Supplementary Methods),3/27/20 10:53:00 AM on a trio of cats from the research colony. The trio included an obligate carrier sire (S13227), a blind queen (S15240) and a female blind offspring (S17799). Seven additional obligate carriers were in the 99 Lives dataset as well as one Bengal cat of unknown status (S20423). An average of ~30X sequencing coverage per cat was achieved.[3] Genome alignment was to cat genome assembly GCF_000181335.3 FELIS_CATUS_9.0, annotation was Ensembl release 94 and variant calling was performed as described[6] and variants were filtered using VarSeq software from Golden Helix (Bozeman, MT). We prioritized variants by their effect on the protein using SnpEff.[7] The GWAS had localized the progressive retinal atrophy locus to cat chromosome A3 (Figure 3A), therefore, we scanned the entire A3 cat chromosome for disease-causing genes and considered all variants that had expected inheritance in the trio, (i.e. homozygous in the two affected cats and heterozygous in the obligate carriers (n = 8; Figure 3A, Table S6). The Bengal cat in the dataset of unknown disease status was excluded from the analysis. We identified only two homozygous variants in the two affected cats, which reside in the genes *CHD6* and *KIF3B*, respectively. All obligate carriers were heterozygous for the *KIF3B* variant. The purebred Bengal cat of unknown status was also heterozygous for the *KIF3B* variant, indicating that this cat was a carrier. The nonsynonymous *KIF3B* change, ENSFCAT00000022266:c.1000G>A, causes a p.Ala334Thr amino acid change, is positioned within the kinesin motor domain (Figure S5), and is predicted to be pathogenic by SIFT[8] and PolyPhen-2[9].

We performed phenotyping at Michigan State University in accordance with an approved institutional animal care and use committee protocol (IACUC; Figure 3B; Supplementary Methods). We reported previously that the first ophthalmoscopic signs of retinal degeneration in affected cats appear at 8 weeks of age, with visual deficits behaviorally evident by 1 year of age. Concordantly, by 8-weeks of age, we observed thinning of the outer retinal layers including the outer nuclear layer (ONL) and loss of definition of the layers representing photoreceptor inner and outer segments (Figure 3B). Immunodetection of Kif3b in the wild-type (WT) animal labelled the inner segment and the inner segment/outer segment junction (Figure 3B; Table S3). In retinal sections from an 8-week-old *KIF3B* mutant, Kif3b was detectable with antibody staining at the inner segments with some mislocalization to the outer portion of the ONL and a blurred demarcation between inner segment and outer segment by comparison to the WT control. However, by 20 weeks of age when the ONL was markedly thinned, Kif3b labeling was barely detectable in mutant felines (Figure 3B). To investigate possible correlates between Kif3b mutation and localization of phototransduction cascade components, we labelled cone markers, ML opsin (MLO) and peanut agglutin (PNA), and a rod marker, rhodopsin Ab-1 (RetP1), respectively (Table S3). At 8 weeks of age, mutant kittens displayed normal cone morphology while there was modest rhodopsin mislocalization to inner segments. By 20 weeks of age, we noted stunting of cone inner and outer segments and marked rod opsin mislocalization to the ONL. At 34 weeks of age, only one or two rows of photoreceptor nuclei remained and we observed loss of cone inner and outer segments with only some material external to the outer limiting membrane still immunopositive for the cone markers; rod opsin mislocalization was still prominent.

A

Visual evoked potential

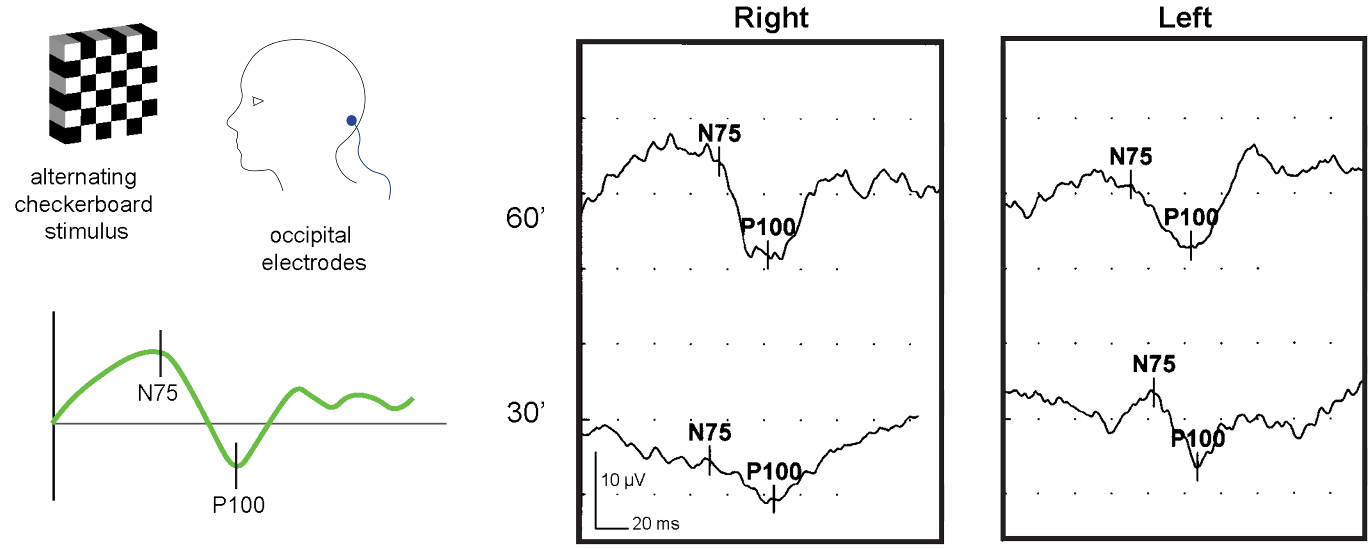

B

Electroretinogram

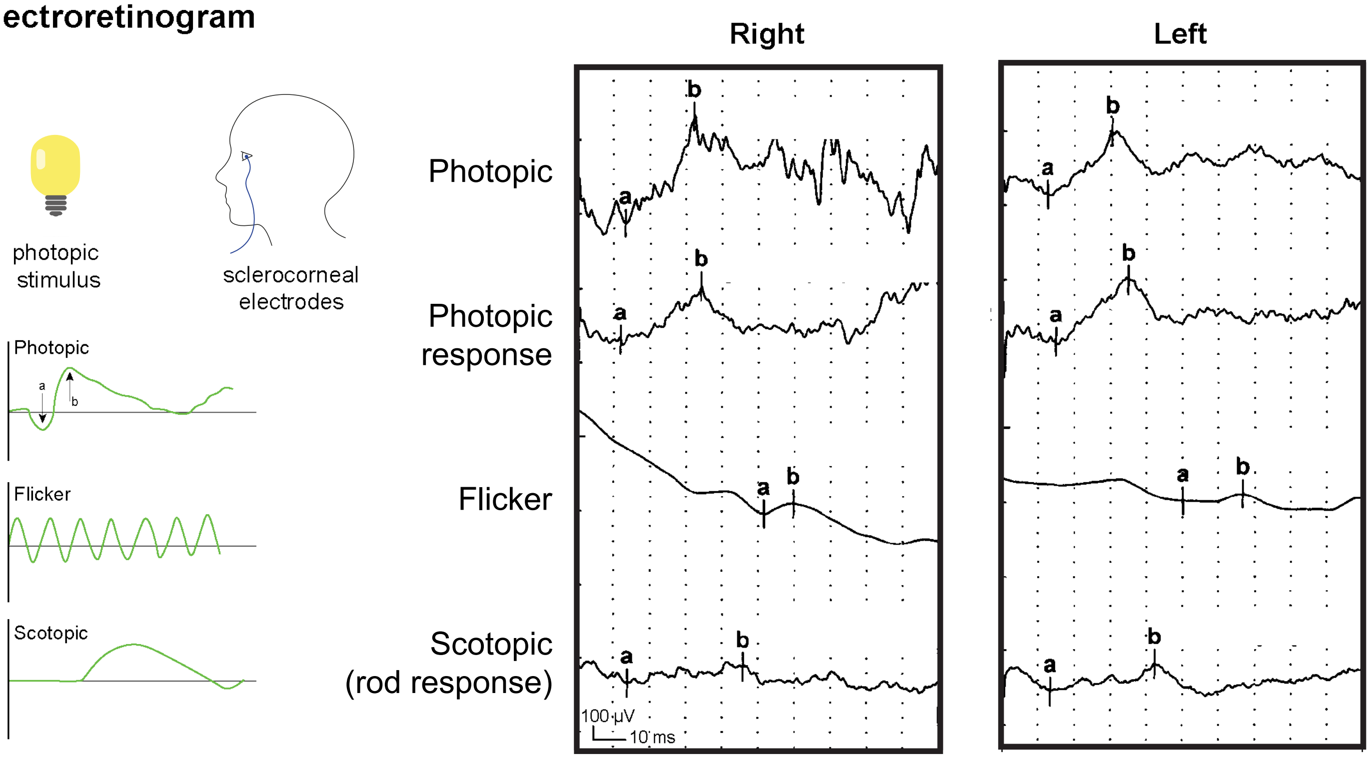

Figure S1

Figure S1. Functional vision evaluation of Individual 1.

(A) Left, recording system and expected result for evoked visual potential. Right, electroretinogram (ERG) of individual 1 (family A) showing an alteration of peripheral retinal responses.

(B) Electroretinogram. Left, recording system and expected result for evoked visual potential. Right, photopic, photopic response, flicker and scotopic response of individual 1. ERG recordings were acquired according to the International Society for Clinical Electrophysiology of Vision (ISCEV) protocol and were performed on a vision monitor (Monpack3, Metrovision, Perenchies, France).

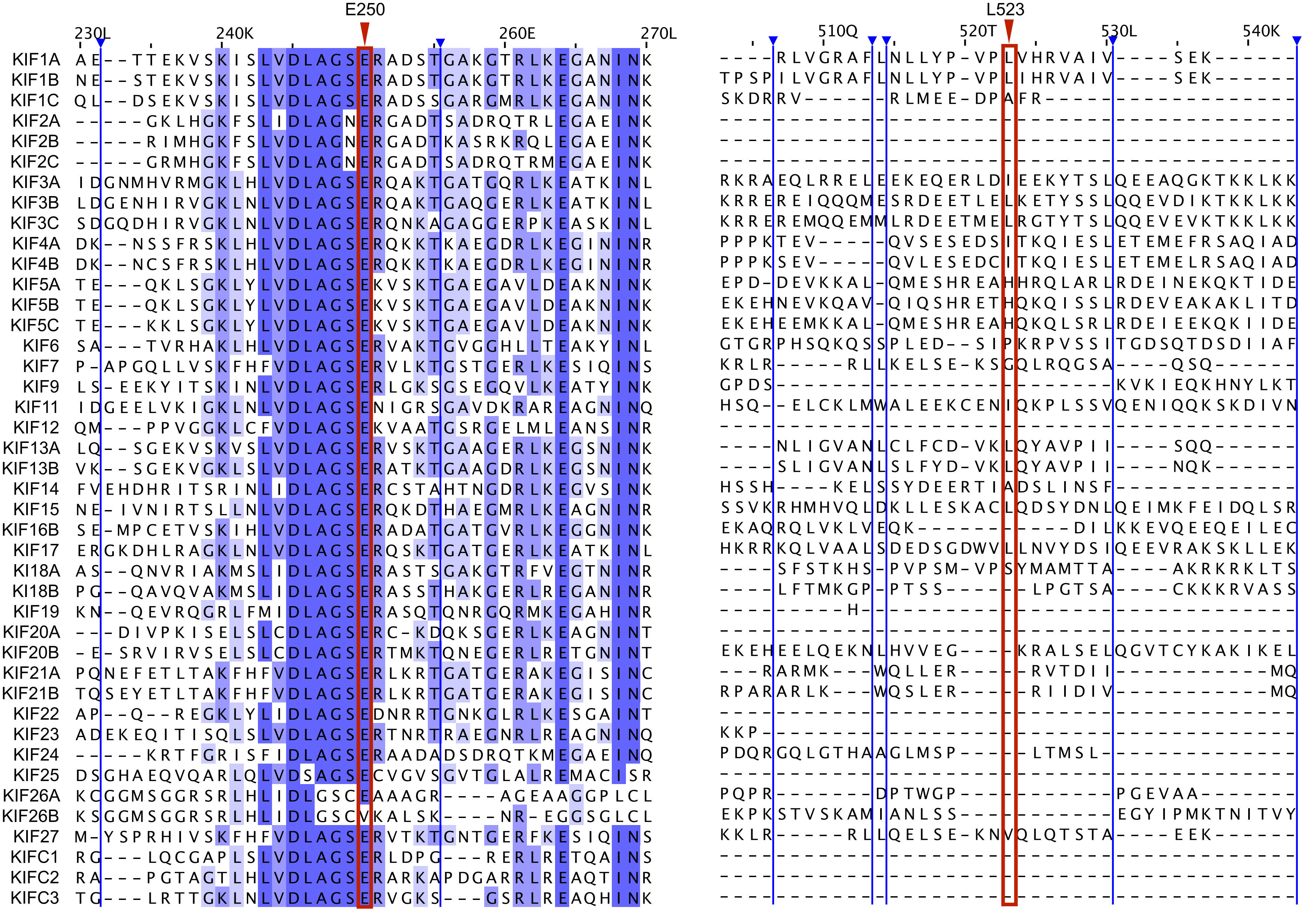
E250
L523
230L
240K
260E
270L
510Q
520T
530L
540K
KIF1A
KIF1B
KIF1C
KIF2A
KIF2B
KIF2C
KIF3A
KIF3B
KIF3C
KIF4A
KIF4B
KIF5A
KIF5B
KIF5C
KIF6
KIF7
KIF9
KIF11
KIF12
KIF13A
KIF13B
KIF14
KIF15
KIF16B
KIF17
KI18A
KI18B
KIF19
KIF20A
KIF20B
KIF21A
KIF21B
KIF22
KIF23
KIF24
KIF25
KIF26A
KIF26B
KIF27
KIFC1
KIFC2
KIFC3

Figure S2

Figure S2. Molecular motor domain residue Glu250 is highly conserved across human kinesins. Multiple-sequence alignment (Clustal O v1.2.4) of 42 human kinesin proteins sorted by pair-wise identity. Color indicates percent identity. Blue arrow head, insertions; red arrow, Glu250 (left) or Leu523 (right) residues. KIF1A: Q12756, KIF1B: O60333, KIF1C: O43896, KIF2A: O00139, KIF2B: Q8N4N8, KIF2C: Q99661, KIF3A: Q9Y496, KIF3B: O15066, KIF3C: O14782, KIF4A: O95239, KIF4B: Q2VIQ3, KIF5A: Q12840, KINH: P33176, KIF5C: O60282, KIF6: Q6ZMV9, KIF7: Q2M1P5, KIF9: Q9HAQ2, KIF11: P52732, KIF12: Q96FN5, KI13A: Q9H1H9, KI13B: Q9NQT8, KIF14: Q15058, KIF15: Q9NS87, KI16B: Q96L93, KIF17: Q9P2E2, KI18A: Q8NI77, KI18B: Q86Y91, KIF19: Q2TAC6, KI20A: O95235, KI20B: Q96Q89, KI21A: Q7Z4S6, KI21B: O75037, KIF22: Q14807, KIF23: Q02241, KIF24: Q5T7B8, KIF25: Q9UIL4, KI26A: Q9ULI4, KI26B: Q2KJY2, KIF27: Q86VH2, KIFC1: Q9BW19, KIFC2: Q96AC6, KIFC3: Q9BVG8.

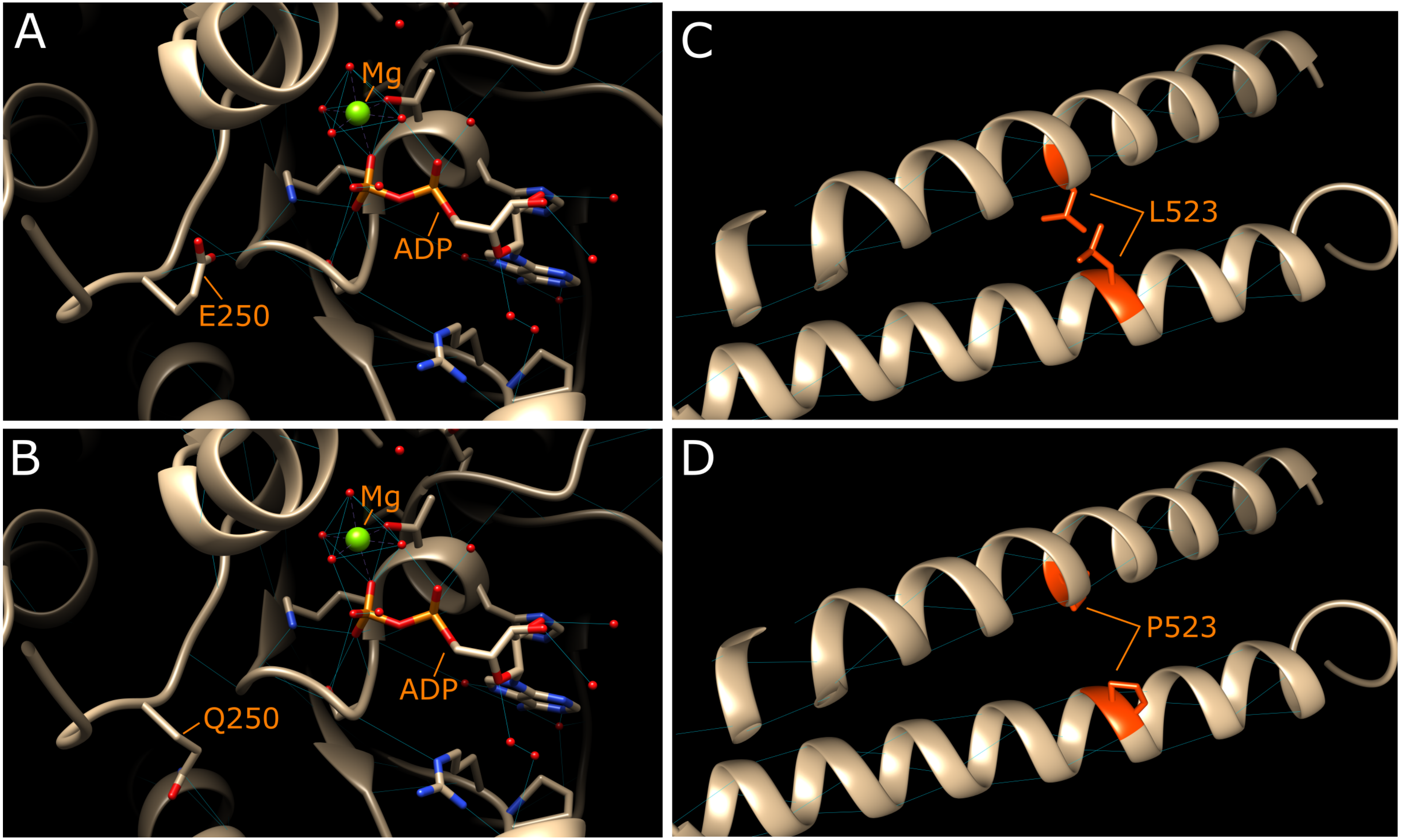

Figure S3

Figure S3. Mutated human KIF3B residues represented on a 3D structure.

(A) The crystallography of the human ubiquitous kinesin motor domain (PDB:1BG2) with magnesium (Mg) and ADP was used to visualize p.Glu250 amino acid. Hydrogen bonds are shown with blue bars. (B) p.Glu250 residue replaced by a Glutamine.

(C) Structure of the KIF3B coiled coil domain was built with SWISS-MODEL as no crystal structure was available for p.Leu523. The corresponding Leucine is depicted.

(D) p.Leu523 residue replaced by a Proline. UCSF chimera software was used for modelling.

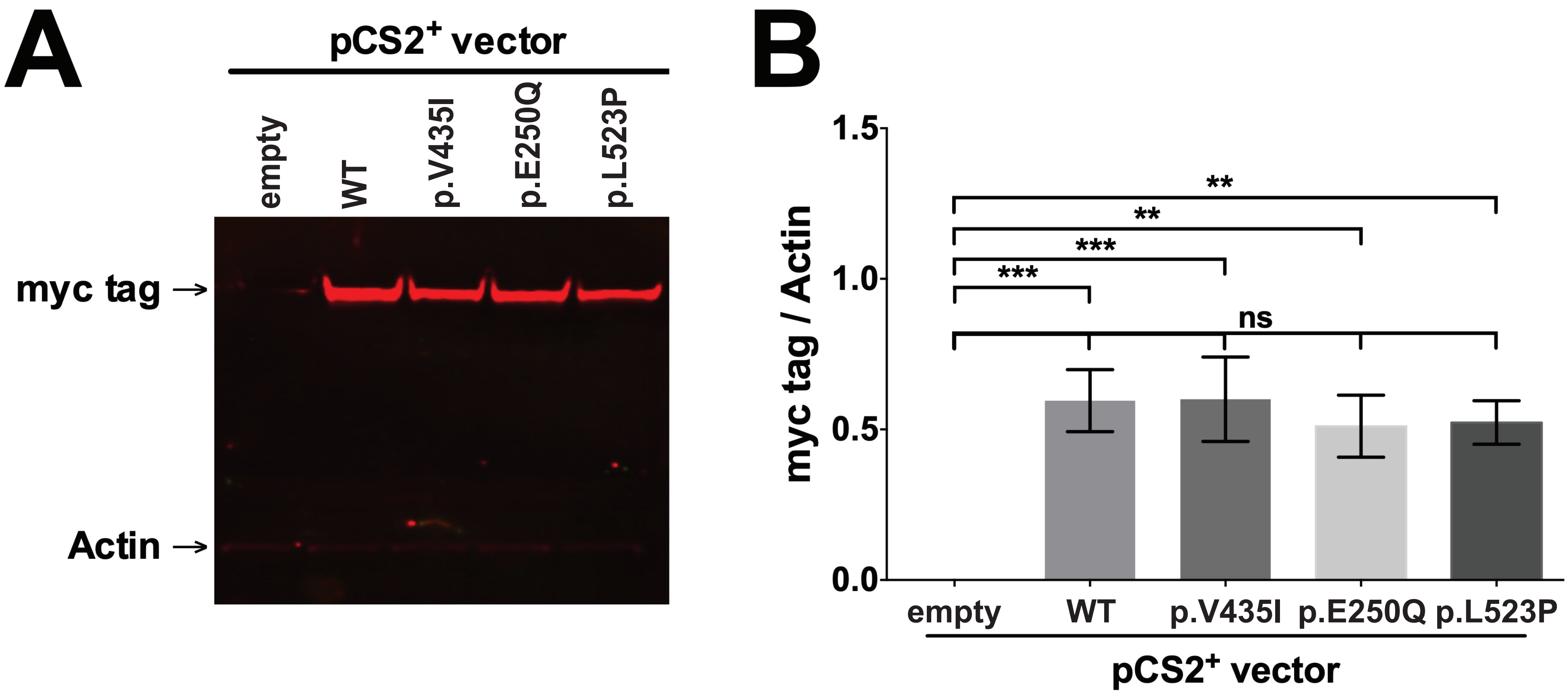
A
pCS2+ vector
empty
WT
p.V435I
p.E250Q
p.L523P
myc tag →
Actin →
B
myc tag / Actin
1.5
1.0
0.5
0.0
**
**
***
***
ns
empty
WT
p.V435I
p.E250Q
p.L523P
pCS2+ vector

Figure S4

Figure S4. Transient expression of KIF3B-myc in HEK293 cells.

(A) Western blot analysis of myc tag (KIF3B expression) and actin in HEK293 cells transiently transfected with pCS2$^+$-empty, pCS2$^+$-*KIF3B-WT-myc*, pCS2$^+$-*KIF3B-V435I-myc*, pCS2$^+$-*KIF3B-E250Q-myc*, pCS2$^+$-*KIF3B-L523P-myc* vectors (48h post transfection).

(B) Quantitative analysis of myc tag (KIF3B expression) normalized to actin in HEK293 cells transiently transfected with pCS2$^+$-empty, pCS2$^+$-*KIF3B-WT-myc*, pCS2$^+$-*KIF3B-V435I-myc*, pCS2$^+$-*KIF3B-E250Q-myc*, pCS2$^+$-*KIF3B-L523P-myc* vectors (48h post transfection). Performed on six independent experiments. Error bars indicate standard error of the mean (s.e.m.).

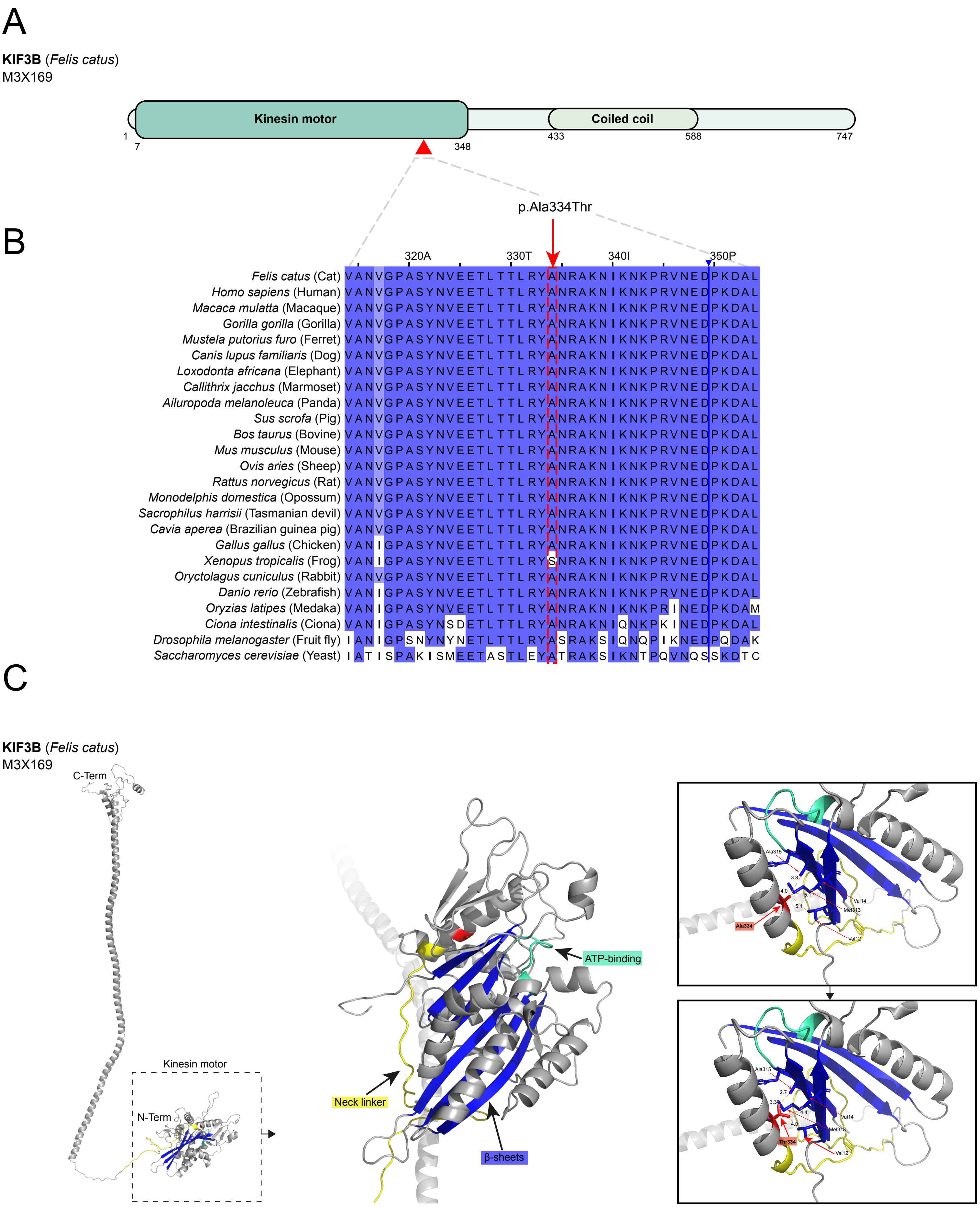
A
KIF3B (*Felis catus*)
M3X169
Kinesin motor
Coiled coil
1
7
348
433
588
747
B
p.Ala334Thr
320A
330T
340I
350P
Felis catus (Cat) VANVGPASYNVEETLTTLRYANRAKNIKNKPRVNEDPKDAL
Homo sapiens (Human) VANVGPASYNVEETLTTLRYANRAKNIKNKPRVNEDPKDAL
Macaca mulatta (Macaque) VANVGPASYNVEETLTTLRYANRAKNIKNKPRVNEDPKDAL
Gorilla gorilla (Gorilla) VANVGPASYNVEETLTTLRYANRAKNIKNKPRVNEDPKDAL
Mustela putorius furo (Ferret) VANVGPASYNVEETLTTLRYANRAKNIKNKPRVNEDPKDAL
Canis lupus familiaris (Dog) VANVGPASYNVEETLTTLRYANRAKNIKNKPRVNEDPKDAL
Loxodonta africana (Elephant) VANVGPASYNVEETLTTLRYANRAKNIKNKPRVNEDPKDAL
Callithrix jacchus (Marmoset) VANVGPASYNVEETLTTLRYANRAKNIKNKPRVNEDPKDAL
Ailuropoda melanoleuca (Panda) VANVGPASYNVEETLTTLRYANRAKNIKNKPRVNEDPKDAL
Sus scrofa (Pig) VANVGPASYNVEETLTTLRYANRAKNIKNKPRVNEDPKDAL
Bos taurus (Bovine) VANVGPASYNVEETLTTLRYANRAKNIKNKPRVNEDPKDAL
Mus musculus (Mouse) VANVGPASYNVEETLTTLRYANRAKNIKNKPRVNEDPKDAL
Ovis aries (Sheep) VANVGPASYNVEETLTTLRYANRAKNIKNKPRVNEDPKDAL
Rattus norvegicus (Rat) VANVGPASYNVEETLTTLRYANRAKNIKNKPRVNEDPKDAL
Monodelphis domestica (Opossum) VANVGPASYNVEETLTTLRYANRAKNIKNKPRVNEDPKDAL
Sacrophilus harrisii (Tasmanian devil) VANVGPASYNVEETLTTLRYANRAKNIKNKPRVNEDPKDAL
Cavia aperea (Brazilian guinea pig) VANVGPASYNVEETLTTLRYANRAKNIKNKPRVNEDPKDAL
Gallus gallus (Chicken) VANIGPASYNVEETLTTLRYANRAKNIKNKPRVNEDPKDAL
Xenopus tropicalis (Frog) VANIGPASYNVEETLTTLRYSNRAKNIKNKPRVNEDPKDAL
Oryctolagus cuniculus (Rabbit) VANVGPASYNVEETLTTLRYANRAKNIKNKPRVNEDPKDAL
Danio rerio (Zebrafish) VANIGPASYNVEETLTTLRYANRAKNIKNKPRVNEDPKDAL
Oryzias latipes (Medaka) VANIGPASYNVEETLTTLRYANRAKNIKNKPRINEDPKDAM
Ciona intestinalis (Ciona) VANIGPASYNSDETLTTLRYANRAKNIQNKPKINEDPKDAL
Drosophila melanogaster (Fruit fly) IANIGPSNYNYNETLTTLRYASRAKSIQNQPIKNEDPQDAK
Saccharomyces cerevisiae (Yeast) IATISPAKISMEETASTLEYATRAKSIKNTPQVNQSSKDTC
C
KIF3B (*Felis catus*)
M3X169
C-Term
Kinesin motor
N-Term
ATP-binding
Neck linker
β-sheets
Ala315
3.8
4.0
5.1
5.1
Val14
Met313
Ala334
Val12
Ala315
2.7
3.3
4.4
4.0
Val14
Met313
Thr334
Val12

Figure S5

Figure S5. Protein structure and amino acid conservation of domestic cat KIF3B p.Ala334Thr.

(A) Schematic of *Felis catus* (cat) KIF3B protein structure. Red arrow head, *KIF3B* c.1000G>A, Ala334Thr variant; Kinesin motor and coiled coil domains (UniProtKB identifier M3X169, PROSITE annotations) are indicated.

(B) *Felis catus* KIF3B protein sequence block impacted by the p.Ala334Thr nonsynonymous change and multiple sequence alignment of 40 amino acid blocks of cat, human and 23 additional species sorted by pairwise identity compared to the human KIF3B protein sequence (Clustal W v1.81). Red box, variant residue; blue shading of amino acids from dark to light represents most to least conserved, respectively. UniProtKB identifiers: *Homo sapiens*, O15066; *Macaca mulatta*, F6S877; *Gorilla gorilla*, G3RAF7; *Mustela putorius furo*, M3Z2F0; *Canis lupus familiaris*, E2QUS2; *Loxodonta africana*, G3T0G8; *Callithrix jacchus*, F7IBN6; *Ailuropoda melanoleuca*, G1M429; *Felis catus*, A0A2I2UKW2; *Sus scrofa*, F1S519; *Bos taurus*, F1N020; *Mus musculus*, Q61771; *Ovis aries*, W5NZV7; *Rattus norvegicus*, D3ZI07; *Monodelphis domestica*, F6RWN1; *Sarcophilus harrisii*, G3WA27; *Cavia aperea*, ENSCAPP00000010080 (ensembl, UniProtKB identifier not available); *Gallus gallus*, Q5F423; *Xenopus tropicalis*, F6R640; *Oryctolagus cuniculus*, G1U1D0; *Danio rerio*, F1QN54; *Oryzias latipes*, H2LAE9; *Ciona intestinalis*, F7B875; *Drosophila melanogaster*, P46867; *Saccharomyces cerevisiae*, P28742.

(C) *In silico* protein modeling of *Felis catus* KIF3B nonsynonymous variant. Left, three dimensional *in silico* view of *Felis catus* KIF3B protein structure (UniProtKB identifier M3X169). Middle, kinesin motor domain impacted by p.Ala334Thr change is shown. Neck linker, ATP-binding and ß-sheets are indicated in yellow, green and blue, respectively. Right, distance (Å) between side chains of wild type (Ala334; upper box) and mutant (Thr334; lower box) KIF3B and the closest residue on the opposing side of the protein are measured as indicated (orange dashed lines). Protein Data Bank (PDB) file was generated by RaptorX and analyzed in Pymol 2.0.

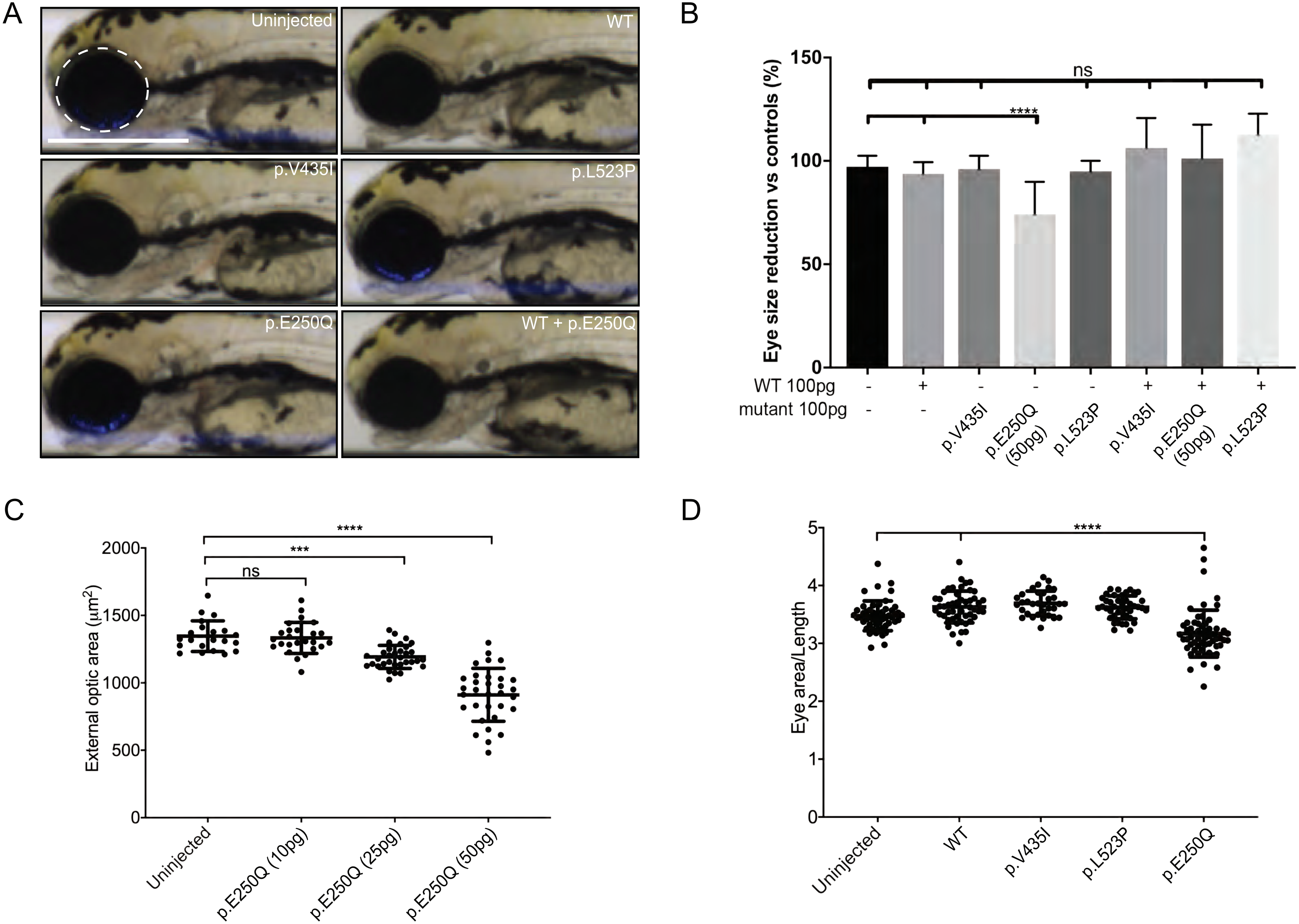
A
Uninjected
WT
p.V435I
p.L523P
p.E250Q
WT + p.E250Q
B
Eye size reduction vs controls (%)
150
100
50
0
ns
****
WT 100pg
mutant 100pg
- - - - - + + +
- - p.V435I p.E250Q (50pg) p.L523P p.V435I p.E250Q (50pg) p.L523P
C
External optic area (μm²)
2000
1500
1000
500
0
ns
***
****
Uninjected
p.E250Q (10pg)
p.E250Q (25pg)
p.E250Q (50pg)
D
Eye area/Length
5
4
3
2
1
0
****
Uninjected
WT
p.V435I
p.L523P
p.E250Q

Figure S6

Figure S6. Eye size in zebrafish larvae with heterologous mutant *KIF3B* expression and normalization of eye size phenotype to zebrafish larval body length.

(A) Representative bright field lateral images of 3-day post fertilization (dpf) larvae captured with the onboard camera attached to the VAST Bioimager system (Union Biometrica). Scale bar: 550 µm, with equivalent scaling for each condition.

(B) Quantification of larval eye area at 3 dpf in the context of human *KIF3B* mRNA (dashed white circle in panel (A). We observed a 20% reduction in mean eye size for p.Glu250Gln mRNA vs WT or uninjected controls. n=50-60 larvae per condition, repeated. Error bars indicate standard deviation (s.d.).

(C) Quantification of external optic area in larval batches injected with a *KIF3B* p.Glu250Gln mRNA dosage curve to determine an optimal dose for phenotyping that does not induce significant lethality at 3 days post fertilization (dpf). See Figure 5A for representative images and region measured. n=60-70 larvae/condition, repeated twice with similar results. Error bars indicate standard deviation (s.d.).

(B) Plot of eye area (µm^2) to body length (µm) ratio to confirm that optic size reduction is not due to developmental delay in *KIF3B* mRNA-injected larvae at 3 dpf.

Non-parametric one-way ANOVA followed by Tukey's multiple comparison (GraphPad PRISM software; version 7.0c). **** $p<0.0001$. ns, not significant; WT, wild type; p.Glu250Gln and p.Leu523Pro are variants identified in cases; p.Val435Ile is a negative control (rs41288638; 230/276,748 alleles in gnomAD). n=40-50 larvae/condition, repeated twice with similar results. Error bars indicate standard deviation (s.d.).

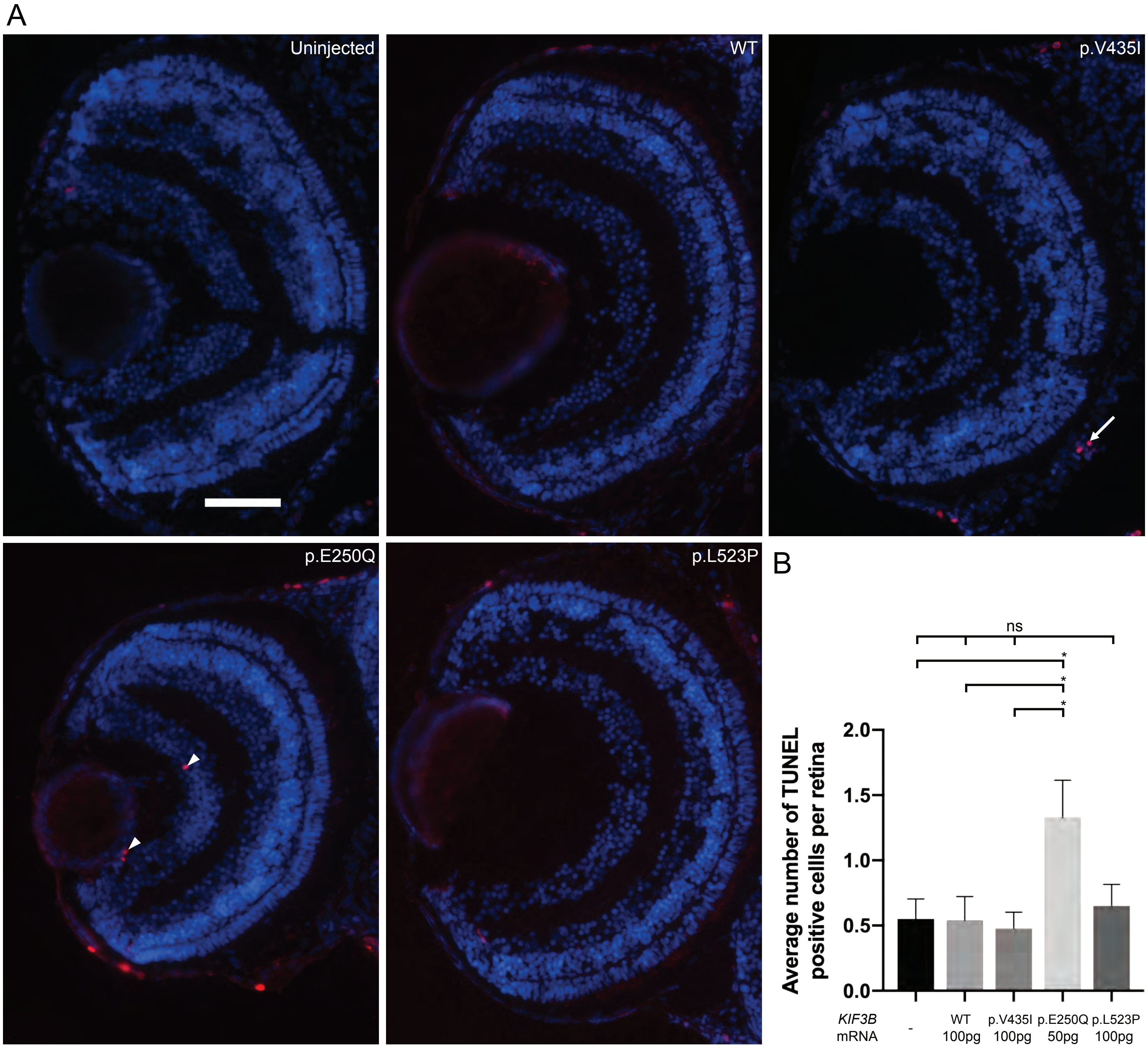
A
Uninjected
WT
p.V435I
p.E250Q
p.L523P
B
ns
*
*
*
2.0
1.5
1.0
0.5
0.0
Average number of TUNEL positive cells per retina
KIF3B mRNA
-
WT 100pg
p.V435I 100pg
p.E250Q 50pg
p.L523P 100pg

Figure S7

Figure S7. Zebrafish larvae injected with mRNA encoding p.Glu250Gln display increased cell death in the retina at 5 dpf.

(A) Representative images of optic sections obtained from 5 dpf larvae and stained with the Apotag Red In situ apoptosis detection kit (Millipore). White arrow heads indicate terminal deoxynucleotidyl transferase dUTP nick-end labeling (TUNEL) positive cells in the retina and the white arrow indicates a TUNEL positive cell outside of the retina (positive control). Scale bar: 50 µm, with equivalent scaling for each condition.

(B) Quantification of TUNEL positive cells at 5 dpf. n=10-13 larvae per condition, repeated twice with similar results. Error bars indicate standard error of the mean (s.e.m.).

Statistical comparison was performed with a non-parametric one-way ANOVA followed by Tukey's multiple comparison (GraphPad PRISM software; version 7.0c). * $p<0.05$. ns, not significant; WT, wild type; p.Glu250Gln and p.Leu523Pro are variants identified in cases; p.Val435Ile is a negative control (rs41288638; 230/276,748 alleles in gnomAD).

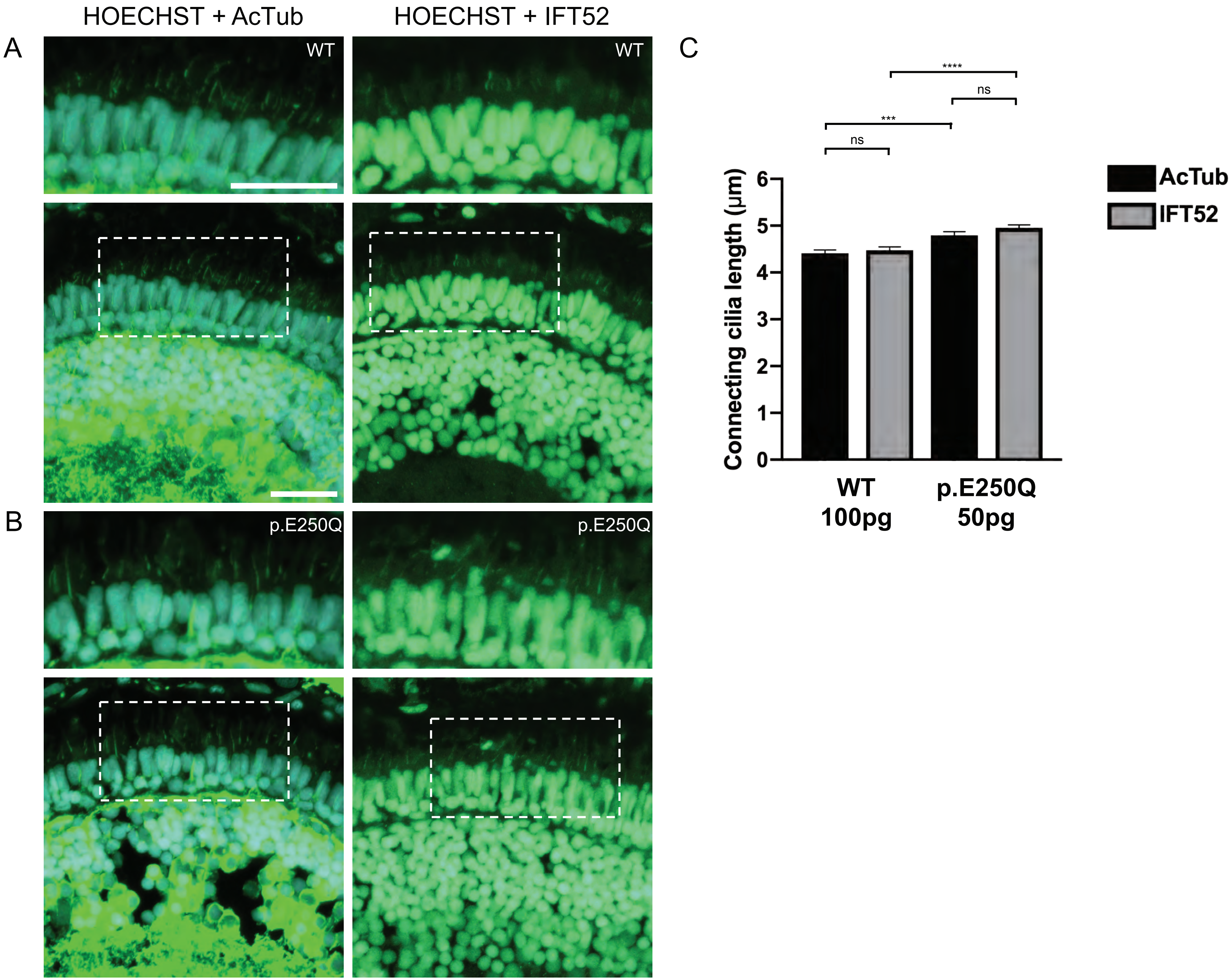
HOECHST + AcTub
HOECHST + IFT52
A
WT
WT
B
p.E250Q
p.E250Q
C
****
ns
***
ns
Connecting cilia length (μm)
0
1
2
3
4
5
6
WT
100pg
p.E250Q
50pg
AcTub
IFT52

Figure S8

Figure S8. Retinal cilia length assessed by either ciliary axoneme or anterograde IFT markers is indistinguishable.

(A) Representative merged images of optic sections obtained from 5 dpf larvae and stained with ciliary markers acetylated α-tubulin mouse monoclonal antibody (AcTub, ciliary axoneme) or anti-IFT52 rabbit polyclonal antibody (anterograde IFT) and Hoechst staining (nuclei); secondary detection was performed with the same fluorophore (Alexa Fluor 488) to test for altered anterograde IFT. Dashed white lines indicate the localization of the insets on top of each picture. Scale bars: 20 μm, with equivalent scaling for each condition.

(B) Quantification of photoreceptor connecting cilia length in 5 dpf zebrafish retinas. n=10-12 larvae per condition, n=97-246 cilia per retina, repeated twice with similar results. Error bars indicate standard error of the mean (s.e.m.). Statistical comparisons were performed with a non-parametric one-way ANOVA followed by Tukey's multiple comparison (GraphPad PRISM software; version 7.0c). ****$p<0.0001$; ns, not significant; WT, wild type; p.Glu250Gln was identified in the family A proband; See Table S3 for antibodies used.

Table S3. Antibodies used to study the effect of KIF3B dysfunction in cells, cat, and zebrafish.

Primary Antibody and Source	Application	Type	Primary Dilution	Secondary Antibody and Source	Secondary Dilution
Arl13b (ADP ribosylation factor like GTPase 13B) 17711-1-AP; Proteintech, Manchester, UK	Cilia marker in primary fibroblasts and hTERT-RPE1 cells	Polyclonal rabbit	1:500	Alexa Fluor 568 or 594 Goat anti-rabbit IgG Life Technologies, Carlsbad, CA, USA	1:1,000
γ-tubulin (gamma tubulin) T6557; Sigma-Aldrich, St. Quentin Fallavier Cedex, France	Centrosome marker in primary fibroblasts and hTERT-RPE1 cells	Monoclonal mouse	1:1,000	Alexa Fluor 488 Goat anti-mouse IgG Life Technologies, Carlsbad, CA, USA	1:1,000
c-myc 9E10; Santa Cruz Biotechnology, Santa Cruz, CA, USA,	IB of protein lysates from HEK293 cells	Monoclonal mouse	1:1,000	IRDyeVR 680RD Goat anti-mouse 925-68070; Li-Cor Biosciences, Lincoln, NE, USA	1:1,000
Actin A2066, Millipore Sigma, St. Louis, MO, USA	IB of protein lysates from HEK293 cells (loading control)	Polyclonal rabbit	1:1,000	IRDyeVR 800CW Goat anti-rabbit 925-32211; Li-Cor Biosciences, Lincoln, NE, USA	1:1,000
Kif3b (Kinesin like-protein 3B) 13817; Cell Signaling, Danvers, MA, USA	IHC in cat retina	Polyclonal rabbit	1:100	Alexa Fluor 488 Goat anti-rabbit IgG Life Technologies, Carlsbad, CA, USA	1:500
ML Opsin (Anti-Opsin, Red/Green; Medium/ Long wavelength cone opsin) AB5405; Millipore Corp., Billerica, MA, USA	IHC in cat retina	Polyclonal rabbit	1:1,000	Alexa Fluor 568 or 594 Goat anti-rabbit IgG Life Technologies, Carlsbad, CA, USA	1:500
PNA (Biotinylated Peanut Agglutinin) B-1075; Vector Labs Inc., Burlingame, CA, USA	IHC in cat retina	Biotinylated Lectin	1:500	Alexa Fluor 488 Streptavadin Life Technologies, Carlsbad, CA, USA	1:500
RetP1 (Rhodopsin Ab-1) MS-1233; Thermo Scientific, Rockford, IL, USA	IHC in cat retina	Monoclonal mouse	1:2	Alexa Fluor 594 Rabbit anti-mouse IgG Life Technologies, Carlsbad, CA, USA	1:500
Rhodopsin MABN15; Millipore Sigma, St. Louis, MO, USA	IHC in zebrafish retina	Monoclonal mouse	1:1,000	Alexa Fluor 488 Goat anti-mouse IgG Life technologies, Carlsbad, CA, USA	1:500
α-acetylated tubulin (alpha acetylated tubulin) T7451, Millipore Sigma, St. Louis, MO, USA	Cilia marker (IHC) in zebrafish retina	Monoclonal mouse	1:1,000	Alexa Fluor 647 Goat anti-rabbit IgG Life Technologies, Carlsbad, CA, USA	1:500
IFT52 (intraflagellar transport 52) gift from Brian Perkins	Anterograde IFT marker (IHC) in zebrafish retina	Polyclonal rabbit	1:5,000	Alexa Fluor 488 Goat anti-rabbit IgG Life Technologies, Carlsbad, CA, USA	1:500

IB, Immunoblotting; IFT, Intraflagellar transport; IHC, Immunohistochemistry

Table S4. Mutagenesis primers used to develop KIF3B mutant plasmids.

KIF3B_748 GC_FOR	cttggcttgccgttggctgccagcaagat
KIF3B_748 GC_REV	atcttgctggcagccaacggcaagccaag
KIF3B_1568 TC_FOR	gagctgtatgtctctttaggttccaaggtctcctcat
KIF3B_1568 TC_REV	atgaggagaccttggaacctaaagagacatacagctc
KIF3B_1303 GA_FOR	catcttctcctctgcaatcaagctgtgatcctcta
KIF3B_1303 GA_REV	tagaggatcacagcttgattgcagaggagaagatg

Table S5. SNPs associated with Bengal Progressive Retinal Atrophy (PRA) from GWAS. *SNP position is based on cat genome assembly FELIS_CATUS_9.0. SNP in bold is closest to *KIF3B*.

SNP Name	Chr	Position*	Association	Bonferroni	Fdr
chrA3.105500036	chrA3	83071208	2.34E-07	0.009966	0.009666
chrA3.104236810	chrA3	82014620	5.87E-07	0.024987	0.009666
chrA3.105245348	chrA3	82843004	6.82E-07	0.028999	0.009666
chrA3.104665241	chrA3	82352814	1.31E-06	0.055786	0.013939
chrUn13.2937466	chrF2	81618955	2.17E-06	0.092295	0.013939
chrA3.106515546	chrA3	83889737	2.23E-06	0.094678	0.013939
chrA3.1044673	**chrA3**	**27964631**	**2.29E-06**	**0.097572**	**0.013939**
chrA3.104098980	chrA3	81904276	6.12E-06	0.260376	0.02928
chrA3.103214225	chrA3	81167532	6.46E-06	0.274758	0.02928
chrA1.124658893	chrA1	1.07E+08	6.88E-06	0.2928	0.02928
chrA3.102843040	chrA3	80870525	1.08E-05	0.457434	0.035045
chrA3.102942692	chrA3	80945609	1.08E-05	0.457434	0.035045
chrA3.141313104	chrA3	1.31E+08	1.14E-05	0.485518	0.035045
chrA3.102918437	chrA3	80925955	1.15E-05	0.490625	0.035045
chrA3.106086700	chrA3	83554809	1.71E-05	0.726363	0.048424
chrA3.102884653	chrA3	80901583	1.95E-05	0.828487	0.049695
chrA3.105824159	chrA3	83341736	2.12E-05	0.902953	0.049695
chrE2.57091972	chrE2	47347454	2.12E-05	0.902953	0.049695
chrA3.101941266	chrA3	80124187	2.30E-05	0.977845	0.049695
chrA3.153780932	chrA3	1.4E+08	2.82E-05	1	0.049695
chrA3.15349133	chrA3	12823090	3.07E-05	1	0.049695
chrA3.147578832	chrA3	1.36E+08	3.07E-05	1	0.049695
chrA3.147780854	chrA3	1.36E+08	3.07E-05	1	0.049695
chrA3.148475337	chrA3	1.36E+08	3.07E-05	1	0.049695
chrA3.149716255	chrA3	1.37E+08	3.07E-05	1	0.049695
chrA3.150600799	chrA3	1.38E+08	3.07E-05	1	0.049695
chrA3.102772524	chrA3	80814167	3.16E-05	1	0.049695
chrUn.22624182	chrB2	51868898	3.27E-05	1	0.049695
chrUn3.2051358	chrA1	1.71E+08	3.63E-05	1	0.05081
chrUn3.2015995	chrA1	1.71E+08	3.63E-05	1	0.05081
chrA3.102974562	chrA3	80975434	3.82E-05	1	0.05081
chrA3.103173709	chrA3	81130065	3.82E-05	1	0.05081
chrA3.134386489	chrA3	1.07E+08	4.45E-05	1	0.054114
chrA3.143059974	chrA3	1.32E+08	4.45E-05	1	0.054114
chrA3.147529959	chrA3	1.35E+08	4.45E-05	1	0.054114

Table S6. Candidate high and moderate effect variants from WGS on cat chromosome A3 (human chromosome 20).

Chromosome Position*	Reference/ Alternative	Alleles	Het	Hom	Gene Name	Variant Effect	Transcript[†]	Amino Acid Effect
A3:18858513	G/A	388	8	2	CHD6	5_prime_UTR_variant	ENSFCAT00000050387:c.-179G>A	
A3:26784019	**C/T**	**390**	**9**	**2**	**KIF3B**	**Missense variant**	**ENSFCAT00000022266:c.1000G>A**	**p.Ala334Thr**
A3:22425011	G/A	390	8	3	SRC	3_prime_UTR_variant	ENSFCAT00000067246:c.*1679C>T	
A3:7014174	A/G	390	9	3	CBLN4	3_prime_UTR_variant	ENSFCAT00000007053:c.544+3527A>G	
A3:23937190	C/T	388	9	3	ERGIC3	Splice region variant	ENSFCAT00000038278:c.368-4G>A	
A3:23889605	G/A	386	9	3	SPAG4	Missense variant	ENSFCAT00000003230:c.259C>T	p.His87Tyr
A3:24057100	-/T	330	10	3	UQCC1	5 prime UTR variant	ENSFCAT00000049200:c.-389dupT	
A3:24003105	T/C	390	10	3	CEP250	Missense variant	ENSFCAT00000003224:c.2069A>G	p.Lys690Arg
A3:23989272	A/G	390	10	3	CEP250	Missense variant	ENSFCAT00000003224:c.3176T>C	p.Ile1059Thr
A3:23983575	G/A	388	10	3	CEP250	Missense variant	ENSFCAT00000003224:c.4178C>T	p.Ala1393Val
A3:23889718	G/A	388	10	3	SPAG4	Missense variant	ENSFCAT00000003230:c.146C>T	p.Pro49Leu
A3:22810151	T/C	388	10	3	SAMHD1	3_prime_UTR_variant	ENSFCAT00000012967:c.*416T>C	

*Positions based on cat reference FELIS_CATUS_9.0. Variant associated with Bengal PRA in bold. Two cats of 195 in the 99 Lives dataset were blind (Hom for homozygous). Eight cats were known obligate carriers and one pedigreed Bengal cat in the dataset was the unexpected carrier (Het for heterozygous). [†]Cat transcript annotation based on Ensembl 94.

Supplementary Methods

Human subjects and whole exome sequencing

Human subjects research was performed in accordance with the local ethics boards at the Nantes University Hospital (Nantes, France) and the University of Texas Health Science Center (Houston, TX, USA).

Family A. We performed whole exome sequencing of the proband with the Agilent SureSelect Clinical Research Exome kit according to manufacturer's instructions and generated 75-bp paired-end reads that were then aligned to human genome hg19 by bwa mem (v0.7.3). We analyzed data following GATK's best practices (v3.4).

Family B. Sample preparation, exome capture, Illumina sequence alignment and variant calling were performed as described.[10]

Plasmids and site directed mutagenesis

We obtained a WT human *KIF3B* open reading frame (ORF) construct (GenBank, NM_004798.4; GeneCopoeia; MO177) and subcloned it into two different Gateway destination vectors: pCS2+-C-myc or pCS2+ using LR clonase II mediated recombination according to manufacturer's instructions (Thermo Fisher). We performed site directed mutagenesis as described,[11] and plasmids were sequence confirmed to ensure ORF integrity.

Cilia length studies in human fibroblasts and hTERT-RPE cells

Cell culture and transient transfections. Fibroblasts were grown following standard procedures in AmnioMAX C-100 Complete Medium at 37°C and 5% CO_2 on labtek slides. hTERT-RPE1 cells were grown following standard procedures in DMEM-F12 Medium at 37°C and 5% CO_2 on labtek slides and transfected with jetPEI (Polyplus transfection®) at 70% confluency. Optimal serum deprivation (24 h) for primary cilium elongation in both cell types was performed.

Immunostaining. Human cultured fibroblasts and hTERT-RPE1 cells (48h post-transfection) were fixed at room temperature for 10 min in methanol (chilled at -20 °C), and then washed with PBS. Samples were permeabilized for 10 min with PBS containing 0.1% Triton-X100 (Sigma-Aldrich), then washed three times for 5 min. Samples were incubated with PBS containing 10% goat serum (Biowest) for 1h at room temperature. Primary antibodies were incubated at 4°C overnight. The primary antibodies mouse IgG1 anti-γ-tubulin (Sigma-Aldrich) and rabbit anti-Arl13b (Proteintech) were used to detect primary cilium morphology (basal body and axoneme, respectively; Table S3). Cells were washed with PBS, and then incubated with goat anti-mouse IgG1 coupled with AlexaFluor 488 (Life Technologies) and anti-rabbit coupled with AlexaFluor 647 (Life Technologies) secondary antibodies for 2h at room temperature in the dark. Samples were washed and mounted with a solution of DAPI-Fluoromount-G® (SouthernBiotech; 00100-20) containing DAPI (4',6'-diamidino-2-phenylindole) for nuclear staining.

Image acquisition and analysis. 3D images of immunostained fibroblasts were captured using a Zeiss LSM700 confocal microscope equipped with a 63x 1.4 numerical aperture oil objective. To compare measured data, all confocal experiments showing ciliary length were acquired in the same conditions using slice thickness of 0.2 μm and a pixel size of 60 nm. Cilia length analysis was based on confocal Z-slices. The first method was used for primary and immortalized cultured cells to measure PC in 3D by Imaris v8.3 software (Bitplane). Serum deprivation allowed a maximal PC-stimulated elongation. This method allowed to normalized genotypes and offered precise value of PC lengths at a time given. In both cases, we double-checked PC length through staining with Arl13b and α-acetylated tubulin. Experiments with fibroblasts were replicated twice, and data were collected from six randomly selected fields imaged on each sample. Experiments with hTERT-RPE1 cells were performed on six independent experiments.

KIF3B Protein stability assays

Cell culture, transient transfections and cycloheximide treatment. HEK293 cells were grown following standard procedures in DMEM Medium at 37°C and 5% CO_2. We transfected cells with jetPEI (Polyplus transfection®) at 70% confluency, and then treated cells with 50 μm cycloheximide for 2h, and 4h post-transfection prior to protein harvest.

Immunoblotting. We prepared HEK293 cell lysates in RIPA buffer supplemented with protease-inhibitor cocktail tablets (cOmplete Mini, EDTA-free, 11836170001, Roche). Protein was migrated on a 4–12% NuPAGE polyacrylamide gel (Life Technologies, NP032B) at 140V for 100 min. The size-separated proteins were transferred to an Immobilon-FL membrane (Merck, IPFL00010) at 20V for 2 hours. After membrane blocking with Odyssey® Blocking Buffer (Li-Cor Biosciences, 927-40000), immunoblots were probed with mouse anti-c-myc and rabbit anti-actin antibodies (Table S3). Secondary detection was accomplished with goat anti-mouse and goat anti-rabbit antibodies using the Li-Cor system (Table S3). The obtained immunoreactivities were determined and calculated with ImageStudioLite software (Li-Cor Biosciences); three (cycloheximide studies) or six (untreated cells) biological replicates were performed for each experiment.

Cat phenotyping

Animals. All procedures were performed in accordance with the Association for Research in Vision and Ophthalmology (ARVO) statement for the Use of Animals in Ophthalmic and Vision Research and were approved by the relevant Institutional Animal Care and Use Committees.

Retinal morphology. Retinal immunohistochemistry (IHC) was performed on *Kif3b* mutant kittens at 8-, 20- and 34-weeks of age and wild type controls at 12-weeks of age. Frozen section immunohistochemistry of retinal cross sections was performed as described[12]. See Table S3 for antibodies used.

Cat genetic evaluations

Genome – wide association study (GWAS). Samples were ascertained as either whole EDTA blood from colony cats or buccal swabs donated by breeders and were prepared for GWAS as described.[1] DNAs from 44 cases and 54 controls were submitted to GeneSeek (Lincoln, NE) for genotyping on the Illumina Infinium iSelect 63K cat DNA array (Illumina, San Diego, CA).[2] GWAS for a case – control autosomal recessive trait was performed as described.[1] SNP genotyping rate and minor allele frequency (MAF) was calculated using PLINK[3]. SNPs with a MAF <5%, genotyping rate <90%, and individuals genotyped for <90% of SNPs were excluded from further analyses. A case-control association analysis was performed and corrected with 10,000 t-max permutations (-mperm 10,000). T-max permuted p-values were considered genome-wide significant at $p<0.05$. A Manhattan plot of the results was generated using HAPLOVIEW[4].

Whole genome sequencing (WGS). DNA for WGS was isolated by organic extraction from ~ 3 ml of EDTA anti-coagulated whole blood that was collected by jugular venipuncture. Approximately 4 µg of high molecular weight DNA from each cat was submitted to the University of Missouri DNA Core for sequencing library preparation and short-read sequencing as described[5]. The 350 bp and 550 bp libraries from all three cats were pooled and analyzed across nine lanes of a HiSeq 2000 (Illumina, Inc.).

Zebrafish phenotyping

Zebrafish husbandry and reagents for microinjection. All zebrafish studies were approved by the Duke University Institutional Animal Care and Use Committee. Zebrafish embryos were obtained by natural mating of wild-type (WT) hybrid TuAB[13] adults that were maintained on a 14h/10h light-dark cycle. Embryos were reared in embryo media (0.3 g/L NaCl, 75 mg/L $CaSO_4$, 37.5 mg/L $NaHC0_3$, 0.003% methylene blue) at 28°C until phenotypic endpoints. To generate variant human mRNA encoding variants identified in cases (p.Glu250Gln, p.Leu523Pro), and the negative control (p.Val435Ile) we performed *in* *vitro* mRNA transcription with the SP6 mMessage mMachine kit (Thermo Fisher) as described (Table S4)[11].

Zebrafish microinjections and phenotyping. We injected embryos at the one-to-four cell stage with human *KIF3B* mRNA (10 pg, 25 pg, 50 pg, or 100 pg). For eye size assessment, we anesthetized larvae with tricaine at 3 days post-fertilization (dpf); imaged them live with the Vertebrate Automated Screening Technology (VAST) Bioimager (Union Biometrica); and measured eye area and body length automatically with FishInspector software[14]. Zebrafish phenotyping was performed with the investigator masked to injection condition, and experiments were repeated at least twice.

Histology of zebrafish retinal sections. We fixed 5 dpf larvae with 4% paraformaldehyde overnight, incubated in 30% sucrose for 24 h, embedded larvae in OCT to generate 7 μm transverse cryosections for the following studies. To evaluate apoptosis, we performed TUNEL detection *in situ* with the ApopTag Red In situ apoptosis detection kit (Millipore) according to manufacturer's instructions. Subsequent to image acquisition with a 90i epifluorescent microscope (Nikon), we counted terminal deoxynucleotidyl transferase dUTP nick-end labeling (TUNEL) positive cells with Image J (NIH). To evaluate photoreceptor integrity in the zebrafish retina, we assessed rhodopsin localization. We performed primary detection with anti-rhodopsin mouse monoclonal antibody (Table S3) essentially as described[15]. Subsequent to image acquisition with a 90i epifluorescent microscope (Nikon), we defined a region of interest corresponding to the rod inner segment (RIS) using Image J (NIH) and measured the mean signal intensity normalized to background (Figure 5B). To measure cilia length in the zebrafish retina, we stained cryosections with anti-acetylated α-tubulin mouse monoclonal antibody and anti-IFT52 rabbit polyclonal antibody (Table S3) as described[16]; nuclei were stained with Hoechst 33342. Z-stack images were acquired with the confocal module of the 90i microscope (90i) and merged in Image J (NIH) using the maximum intensity function. Connecting cilia were highlighted by both antibodies and measured using the segmented line tool.

Statistical comparisons.

Statistical comparisons were performed with two-tailed unpaired t-test (densitometry of immunoblotting) or a non-parametric one-way ANOVA followed by Tukey's multiple comparison (cilia length in cells; eye size, body length, cilia length or apoptosis in zebrafish) using GraphPad PRISM software. Significance was defined as $p<0.05$.

References

1. Ofri, R., Reilly, C.M., Maggs, D.J., Fitzgerald, P.G., Shilo-Benjamini, Y., Good, K.L., Grahn, R.A., Splawski, D.D., and Lyons, L.A. (2015). Characterization of an Early-Onset, Autosomal Recessive, Progressive Retinal Degeneration in Bengal Cats. Invest. Ophthalmol. Vis. Sci. *56*, 5299–5308.

2. Gandolfi, B., Grahn, R.A., Creighton, E.K., Williams, D.C., Dickinson, P.J., Sturges, B.K., Guo, L.T., Shelton, G.D., Leegwater, P.A.J., Longeri, M., et al. (2015). COLQ variant associated with Devon Rex and Sphynx feline hereditary myopathy. Anim. Genet. *46*, 711–715.

3. Oh, A., Pearce, J.W., Gandolfi, B., Creighton, E.K., Suedmeyer, W.K., Selig, M., Bosiack, A.P., Castaner, L.J., Whiting, R.E.H., Belknap, E.B., et al. (2017). Early-Onset Progressive Retinal Atrophy Associated with an IQCB1 Variant in African Black-Footed Cats (Felis nigripes). Sci. Rep. *7*, 43918.

4. Lyons, L.A., Creighton, E.K., Alhaddad, H., Beale, H.C., Grahn, R.A., Rah, H., Maggs, D.J., Helps, C.R., and Gandolfi, B. (2016). Whole genome sequencing in cats, identifies new models for blindness in AIPL1 and somite segmentation in HES7. BMC Genomics *17*, 265.

5. Aberdein, D., Munday, J.S., Gandolfi, B., Dittmer, K.E., Malik, R., Garrick, D.J., Lyons, L.A., and 99 Lives Consortium (2017). A FAS-ligand variant associated with autoimmune lymphoproliferative syndrome in cats. Mamm. Genome Off. J. Int. Mamm. Genome Soc. *28*, 47–55.

6. Lyons, L.A., Fox, D.B., Chesney, K.L., Britt, L.G., Buckley, R.M., Coates, J.R., Gandolfi, B., Grahn, R.A., Hamilton, M.J., Middleton, J.R., et al. (2019). Localization of a feline autosomal dominant dwarfism locus: a novel model of chondrodysplasia. BioRxiv 687210.

7. Cingolani, P., Platts, A., Wang, L.L., Coon, M., Nguyen, T., Wang, L., Land, S.J., Lu, X., and Ruden, D.M. (2012). A program for annotating and predicting the effects of single nucleotide polymorphisms, SnpEff: SNPs in the genome of Drosophila melanogaster strain w1118; iso-2; iso-3. Fly (Austin) *6*, 80–92.

8. Kumar, P., Henikoff, S., and Ng, P.C. (2009). Predicting the effects of coding non-synonymous variants on protein function using the SIFT algorithm. Nat. Protoc. *4*, 1073–1081.

9. Adzhubei, I.A., Schmidt, S., Peshkin, L., Ramensky, V.E., Gerasimova, A., Bork, P., Kondrashov, A.S., and Sunyaev, S.R. (2010). A method and server for predicting damaging missense mutations. Nat. Methods *7*, 248–249.

10. Koboldt, D.C., Larson, D.E., Sullivan, L.S., Bowne, S.J., Steinberg, K.M., Churchill, J.D., Buhr, A.C., Nutter, N., Pierce, E.A., Blanton, S.H., et al. (2014). Exome-based mapping and variant prioritization for inherited Mendelian disorders. Am. J. Hum. Genet. *94*, 373–384.

11. Niederriter, A.R., Davis, E.E., Golzio, C., Oh, E.C., Tsai, I.-C., and Katsanis, N. (2013). In vivo modeling of the morbid human genome using Danio rerio. J. Vis. Exp. JoVE e50338.

12. Mowat, F.M., Gornik, K.R., Dinculescu, A., Boye, S.L., Hauswirth, W.W., Petersen-Jones, S.M., and Bartoe, J.T. (2014). Tyrosine capsid-mutant AAV vectors for gene delivery to the canine retina from a subretinal or intravitreal approach. Gene Ther. *21*, 96–105.

13. Nasiadka, A., and Clark, M.D. (2012). Zebrafish breeding in the laboratory environment. ILAR J. *53*, 161–168.

14. Teixidó, E., Kießling, T.R., Krupp, E., Quevedo, C., Muriana, A., and Scholz, S. (2019). Automated Morphological Feature Assessment for Zebrafish Embryo Developmental Toxicity Screens. Toxicol. Sci. Off. J. Soc. Toxicol. *167*, 438–449.

15. Liu, Y.P., Bosch, D.G.M., Siemiatkowska, A.M., Rendtorff, N.D., Boonstra, F.N., Möller, C., Tranebjærg, L., Katsanis, N., and Cremers, F.P.M. (2017). Putative digenic inheritance of heterozygous RP1L1 and C2orf71 null mutations in syndromic retinal dystrophy. Ophthalmic Genet. *38*, 127–132.

16. Krock, B.L., and Perkins, B.D. (2008). The intraflagellar transport protein IFT57 is required for cilia maintenance and regulates IFT-particle-kinesin-II dissociation in vertebrate photoreceptors. J. Cell Sci. *121*, 1907–1915.